Searching for modified gravity: scale and redshift dependent constraints from galaxy peculiar velocities

Andrew Johnson,[1,2]★ Chris Blake,[1] Jason Dossett,[3] Jun Koda,[3] David Parkinson[4] and Shahab Joudaki[1]

[1]*Centre for Astrophysics & Supercomputing, Swinburne University of Technology, PO Box 218, Hawthorn, VIC 3122, Australia*
[2]*ARC Centre of Excellence for All-sky Astrophysics (CAASTRO)*
[3]*INAF – Osservatorio Astronomico di Brera, via Emilio Bianchi 46, I-23807 Merate, Italy*
[4]*School of Mathematics and Physics, University of Queensland, Brisbane, QLD 4072, Australia*

ABSTRACT

We present measurements of both scale- and time-dependent deviations from the standard gravitational field equations. These late-time modifications are introduced separately for relativistic and non-relativistic particles, by way of the parameters $G_{matter}(k, z)$ and $G_{light}(k, z)$ using two bins in both scale and time, with transition wavenumber 0.01 Mpc^{-1} and redshift 1. We emphasize the use of two dynamical probes to constrain this set of parameters, galaxy power-spectrum multipoles and the direct peculiar velocity power spectrum, which probe fluctuations on different scales. The multipole measurements are derived from the WiggleZ and Baryon Oscillation Spectroscopic Survey (BOSS) CMASS galaxy redshift surveys and the velocity power spectrum is measured from the velocity sub-sample of the 6-degree Field Galaxy Survey. We combine these measurements with additional cosmological probes. Using a Markov Chain Monte Carlo likelihood analysis, we find the inferred best-fitting parameter values of $G_{matter}(k, z)$ and $G_{light}(k, z)$ to be consistent with the standard model at the 95 per cent confidence level. We expand this analysis by performing Bayesian model selection between our phenomenological model and general relativity. Using the evidence ratio we find 'no support' for including modifications to general relativity. Furthermore, accounting for the Alcock–Paczynski effect, we perform joint fits for the expansion history and growth index gamma; we measure $\gamma = 0.665 \pm 0.067$ (68 per cent CL) for a fixed expansion history, and $\gamma = 0.73^{+0.08}_{-0.10}$ (68 per cent CL) when the expansion history is allowed to deviate from Λ cold dark matter. For the latter case, we observe a 2σ tension with the standard model where $\gamma = 0.554$.

Key words: surveys – cosmological parameters – cosmology: observations – dark energy.

1 INTRODUCTION

The observation of an accelerating cosmic expansion rate has likely provided an essential clue for advancing our theories of gravitation and particle physics (Witten 2001). Interpreting and understanding this feature of our Universe will require both observational and theoretical advancement. Observationally it is critical that we both scrutinize the standard vacuum energy interpretation and thoroughly search for unexpected features resulting from exotic physics. Such features may exist hidden within the clustering patterns of galaxies, the coherent distortion of distant light rays, and the local motion of galaxies; searching for these features is the goal we pursue herein.

Either outcome will facilitate progress: failure to detect unexpected features, confirming a truly constant vacuum energy, will give credence to anthropic arguments formulated within String Theory (Susskind 2003). New observational signatures should then be targeted (e.g. Bousso, Harlow & Senatore 2013). Alternatively, an observed deviation from a cosmological constant would indicate a new dynamical dark energy (DE) component or a modification to Einstein's field equations (Copeland, Sami & Tsujikawa 2006; Clifton et al. 2012). Independent of observational progress, historical trends in science may offer an independent tool to predict the fruitfulness of each interpretation (Lahav & Massimi 2014).

The possibility of new physics explaining the accelerating expansion has inspired an impressive range of alternative models. As such, a detected deviation from the standard model will not present a clear direction forwards, that is, interpreting such a deviation will be problematic. One potential solution, which we adopt, is to

★E-mail: asjohnson@swin.edu.au

analyse observations within a phenomenological model that captures the dynamics of a large range of physical models (e.g. Bean & Tangmatitham 2010; Daniel et al. 2010; Simpson et al. 2013). It should be noted that not all approaches that introduce modified gravity (MG) or DE invoke an artificial separation between the cosmological constant problem and the problem of an accelerating expansion (e.g. Copeland, Padilla & Saffin 2012).

To characterize the usefulness of phenomenological models we consider their ability to describe known physical models: namely, their commensurability (Kuhn 1970). This property can be understood as describing the degree to which measurements made in one model can be applied to others. The absence of this property implies that a measurement should only be interpreted in terms of the adopted model: a consistency test. Whereas given this property one can constrain a range of models simultaneously, alleviating the problem of having to re-analyse each model separately.

Specifically, the model we adopt allows extensions to the standard Λ cold dark matter (ΛCDM) model by introducing general time- and scale-dependent modifications (G_{light} and G_{matter}) to General Relativity (Daniel et al. 2010): these parameters vary the relationship between the metric and density perturbations (i.e. they act as effective gravitational coupling). In this case, the equivalence between the spatial and temporal metric perturbations is not imposed. The commensurability of our model to others can then be shown by proving that G_{light} and G_{matter} capture all the new physics in specific MG scenarios.

For example, de Felice, Kase & Tsujikawa (2011) show that by introducing parameters equivalent to G_{light} and G_{matter} one can provide an effective description of the entire Horndeski class of models. Importantly, the Horndeski class of models contains the majority of the viable DE and MG models (Deffayet et al. 2011; Silvestri, Pogosian & Buniy 2013). An often disregarded caveat is that the mappings between these gravitational parameters and MG and DE theories are only derived at linear order. Therefore, until proved otherwise, the ability of the phenomenological models to describe physical models is lost when using observations influenced by non-linear physics. To avoid this reduction in applicability we will focus on observations in the linear regime. We note this point has been emphasized elsewhere by, for example, Linder & Cahn (2007) and Samushia et al. (2014).

In pursuit of deviations from the standard model we use a range of cosmological observations. In particular, two dynamical probes will be emphasized: the galaxy multipole power spectrum and velocity power spectrum (for example, Beutler et al. 2014; Johnson et al. 2014). Hitherto, in the context of phenomenological models with scale-dependence, neither probe has been analysed self-consistently. In addition we utilize the following cosmological probes: baryon acoustic oscillations, Type Ia SNe, the cosmic microwave background (CMB), lensing of the CMB, and temperature–galaxy cross-correlation (this correlation is caused by the integrated Sachs–Wolf effect, ISW).

We adopt this combination of probes, direct peculiar velocities (PVs) and redshift–space distortions (RSDs), to maximize our sensitivity to a range of length-scales. This range is extended as the sensitivity of both measurements is relatively localized at different length-scales: RSDs at small scales, and peculiar velocity measurement at large scales (Dodelson 2003). The benefit is an increased sensitivity to scale-dependent modifications. The properties of, and physical motivations for, scale-dependent modifications to GR are discussed by Silvestri et al. (2013) and Baker et al. (2014).

In Section 2, we summarize the adopted phenomenological models and further motivate their use. Then in Section 3, we outline the

primary data sets used along with the methodology we use to analyse them. Section 4 then presents the secondary data sets we employ. The results and interpretations of the Markov Chain Monte Carlo (MCMC) analysis are presented in Section 5, and the conclusions are outlined in Section 6.

2 MODIFIED GROWTH AND EVOLUTION

2.1 Introduction

Working within the conformal Newtonian gauge, perturbations to the Robertson–Walker metric can be characterized by two scalar potentials. One scalar potential describes a temporal perturbation to the metric ψ, the other a spatial perturbation, ϕ. The line element in this case is given by

$$ds^2 = a^2[-(1 + 2\psi)d\tau^2 + (1 - 2\phi)d\vec{x}^2] , \tag{1}$$

where a is the scale factor, τ is the conformal time – related to the proper time of comoving observers by $\tau = \int dt/a(t)$ – and $\boldsymbol{x}$ the spatial coordinate. A non-relativistic fluid within this space–time is characterized in terms of a velocity divergence $\theta(\boldsymbol{x}, \tau)$ and a density perturbation $\delta\rho(\boldsymbol{x}, \tau)$. The cosmic evolution of this fluid is then determined by its coupling to the metric potentials.

We concentrate on modifying two of the four gravitational field equations, by requiring energy-momentum conservation ($\nabla^\mu T_{\mu\nu} = 0$), or equivalently, by requiring the contracted Bianchi identity to hold, i.e. $\nabla^\mu G_{\mu\nu} = 0$. Enforcing either constraint one finds the relativistic continuity and Euler equations in Fourier space:

$$\dot{\delta}_m = -\theta_m + 3\dot{\phi}, \tag{2}$$

$$\dot{\theta}_m = -\mathcal{H}\theta_m + k^2\psi , \tag{3}$$

where $\delta_m \equiv \delta\rho_m/\bar{\rho}_m$ and $\mathcal{H} \equiv \dot{a}/a = (da/d\tau)/a$, and $\bar{\rho}_m$ is the background matter density. This system of four variables can then be closed by specifying the gravitational field equations; in particular, by defining the relationship between the two metric potentials, and the coupling between the metric potentials and the matter overdensity. In GR these relationships are given by

$$\nabla^2\psi = 4\pi G_N a^2 \bar{\rho}_m \Delta_m \tag{4}$$

$$\phi = \psi , \tag{5}$$

where G_N is Newton's gravitational constant, and the equations are defined in terms of the comoving-gauge density perturbation $\Delta_m = \delta_m + (3\mathcal{H}/k^2)\theta_m$.

2.2 $G_{light}(k, z)$ and $G_{matter}(k, z)$

We now introduce two dimensionless free parameters G_{light} and G_{matter} that we use to model deviations to the field equations. Our model is now specified as (Daniel & Linder 2013)

$$\nabla^2\psi = 4\pi G_N a^2 \bar{\rho}_m \Delta_m \times G_{matter} \tag{6}$$

$$\nabla^2(\phi + \psi) = 8\pi G_N a^2 \bar{\rho}_m \Delta_m \times G_{light} . \tag{7}$$

The first equation governs the motion of non-relativistic particles, while the second controls the propagation of light along null geodesics. As a result, G_{matter} can be measured using RSDs and direct PVs, and G_{light} can be measured using weak lensing. Because of this distinction the two parameters are significantly less correlated

than models involving a 'slip' relation (e.g. Bean & Tangmatitham 2010). Note that the variables $\{\Sigma, \mu\}$ in Simpson et al. (2013) and Zhao et al. (2012) are equivalent to $\{G_{light}, G_{matter}\}$. There is also a trivial re-mapping to the $\{Q, R\}$ parameters used by Bean & Tangmatitham (2010), through $G_{matter} = QR$, $G_{light} = Q(1 + R)/2$.

To ensure our model can test for a variety of deviations from GR we allow for both scale- and redshift-dependence: that is, $G_{light} = G_{light}(z, k)$ and $G_{matter} = G_{matter}(z, k)$. To specify these parameters we use a high versus low-redshift, large versus small scale binning approach introduced by Daniel & Linder (2010). Note, however, that very general functional forms for these parameters (including scale-dependent terms) have been developed (Silvestri et al. 2013; Baker et al. 2014). We leave such investigations to future work.

Our adopted model introduces eight free parameters and requires one to specify a redshift and wavenumber transition scale, z_t and k_t. We set $z_t = 1$ and $k_c = 0.01\,\mathrm{Mpc}^{-1}$; therefore, we have two redshift bins (viz., $0 < z < 1$ and $1 < z < 2$) and two wavenumber bins ($10^{-4}\mathrm{Mpc}^{-1} < k < 10^{-2}\mathrm{Mpc}^{-1}$ and $0.01\,\mathrm{Mpc}^{-1} < k < 0.1\,\mathrm{Mpc}^{-1}$), while for $z > 2$ and $k < 10^{-4}\mathrm{Mpc}^{-1}$ GR is restored. The transition between bins is implemented using an arctan function of width $\Delta z = 0.05$ and $\Delta k = 0.001\,\mathrm{Mpc}^{-1}$.

The choice of the bin transitions $k = 0.01\,\mathrm{Mpc}^{-1}$ and $z = 1$ follows Daniel & Linder (2010, 2013). These values are motivated by the sensitivity in both redshift and wavenumber of the available data; for example, the PV measurements add constraints at $k < 0.01\,\mathrm{Mpc}^{-1}$ while RSDs add constraints at $k > 0.01\,\mathrm{Mpc}^{-1}$. Furthermore, the redshift deviation is limited to lower redshifts (i.e. $z \leq 2$) given the precision of current CMB constraints.

For our first model, we choose to leave the cosmic expansion unmodified at the ΛCDM prediction, and concentrate on the growth of structure. Henceforth, we will refer to this model as model I. To calculate the relevant observables (to be discussed in the next section) we use CAMB and COSMOMC. The modified field equations (equation 7) are incorporated into CAMB using the publicly available code ISITGR (Dossett, Ishak & Moldenhauer 2011), and the exact equations implemented in CAMB are given by Dossett et al. (2011). Note the only significant difference between the equations employed in CAMB and equation (7) is that the latter are written within the synchronous gauge (Ma & Bertschinger 1995).

A few technical comments on the model are unavoidable: First, superhorizon curvature perturbations need to be conserved independent of the form of field equations (Bertschinger & Zukin 2008). This condition was shown to be satisfied for this model by Pogosian et al. (2010). Additionally, it is natural to include a smoothness theory prior on these parameters, however, given the large distance between the centre of our bins we choose not to include such a prior (Silvestri et al. 2013). With more accurate data, and hence a larger number of bins, this argument will no longer be valid. Finally, the accuracy of any mapping from our model to physical models (i.e. those derived from an action) relies on the validity of the quasi-static approximation (QSA). Following the arguments presented in Silvestri et al. (2013) it is reasonable to include a theoretical prior to ignore such deviations.

2.3 Varying growth and expansion: $\{\gamma, w_0, w_a\}$

As more freedom is introduced to model deviations from GR the precision of the inferred parameters degrades. We must decide then which features of the standard model to preserve; for example, to what extent does the expansion history dictate the growth history. This presents a balancing problem with no clear solution. To partially circumvent this issue we adopt a second model (which we label model II). In contrast to our first model, this model includes only minimal extensions to the standard model. As a result there are fewer free parameters and more precise tests are possible (although we none the less introduce deviations to both the expansion and growth history).

This minimal extension to the standard model using the parameters $\{w_0, w_a, \gamma\}$ has been advocated by Linder & Cahn (2007), Linder (2005), and Simpson & Peacock (2010), and applications have been presented, for example, by Huterer & Linder (2007). To expand on this, we introduce deviations to the expansion history through a time-dependent equation of state $w(z)$, which is expressed in terms of two free parameters: $w_0 = w(a = 0)$ and $w_a = -(dw/da)|_{a=1}$, as a function of the redshift $w(z) = w_0 + w_a z/(1 + z)$. Note the expansion history is still governed by the Friedman equation, there is simply more freedom in the properties of the DE component. We introduce deviations in the growth history by parameterizing the growth rate as $f(z) \equiv \Omega_m(z)^\gamma$, where γ is the growth index; within GR one expects $\gamma \sim 0.55$. The growth rate is defined by $f(a) \equiv d\ln D(a)/d\ln a$, and $D(a) \equiv \delta(a)/\delta(a = 1)$.

3 PRIMARY DATA SETS: METHODOLOGY

Below we will outline the measurements we use in Section 5, in addition to the tools we use to analyse them. A general summary is provided in Table 1 where the data sets, the measured quantities, and the fitting ranges adopted are specified. The focus will be on introducing extensions to the public MCMC code COSMOMC (Lewis & Bridle 2002) and CAMB (Lewis, Challinor & Lasenby 2000) to update the range of data sets one can analyse.

3.1 Velocity power spectrum

The radial PVs of galaxies in the local universe induce a fluctuation in the apparent magnitude m, defined as (Hui & Greene 2006)

$$\delta m(z) = [m(z) - \bar{m}(z)]. \tag{8}$$

The overbar indicates that the variable is being evaluated within a homogeneous universe, namely, a universe with no density gradients and therefore no PVs. Recall the apparent magnitude is defined as

$$m = M + 5\log_{10}(D_L(z)) + 25. \tag{9}$$

Here M is the absolute magnitude, and $D_L(z)$ the luminosity distance. The presence of large-scale clustering induces fluctuations in $\delta m(z)$ from galaxy to galaxy (this is equivalent to a PV), furthermore, these fluctuations are correlated for nearby galaxies (Hui & Greene 2006; Gordon, Land & Slosar 2007). The magnitude of both effects can be described by a covariance matrix which we define as $C_{ij}^m \equiv \langle \delta m_i(z_i) \delta m_j(z_j) \rangle$. Once a model is specified this covariance matrix can be calculated as

$$C_{ij}^m = G(z_i, z_j) \int \frac{dk}{2\pi^2} k^2 \mathcal{P}_{vv}(k, a = 1) W(k, \alpha_{ij}, r_i, r_j), \tag{10}$$

where $\mathcal{P}_{vv}(k) = \mathcal{P}_{\theta\theta}(k)/k^2$ is the velocity power spectrum, and $\theta = \nabla \cdot \boldsymbol{v}$ is the velocity divergence. Moreover, the window function is defined as

$$W(k, \alpha_{ij}, r_i, r_j) = 1/3 \left[j_0(kA_{ij}) - 2j_2(kA_{ij}) \right] \hat{r}_i \cdot \hat{r}_j$$
$$+ \frac{1}{A_{ij}^2} j_2(kA_{ij}) r_i r_j \sin^2(\alpha_{ij}),$$

Table 1. Summary of the data sets used in this analysis. Given model I includes scale-dependent terms, we divide our measurements into three separate groups: those used to constrain model I and II, only model I, and only model II. This division is indicated by the horizontal lines, and follows the order in which the categories were introduced.

Cosmological probe	Data set	Measured quantity	Reference
CMB temperature	*Planck*	C_l^{TT}	Planck Collaboration XVI (2014c)
CMB polarization	*WMAP*-9	C_l^{EE}	Bennett et al. (2013)
CMB-lensing	*Planck*	$C_l^{\phi\phi}$	Planck Collaboration XVI (2014a)
BAOs	6dFGS	$r_s/D_V(z)$	Beutler et al. (2011)
....	BOSS DR11 LOWZ	$D_V(r_s^{\rm fid}/r_s)$	Anderson et al. (2014a)
....	BOSS DR11 QSA-Ly α	$H(z)r_s, D_A/r_s$	Font-Ribera et al. (2014)
....	BOSS DR11 Ly α	$H(z)r_s, D_A/r_s$	Delubac et al. (2014)
Type Ia Supernovae.........	SNLS	$\mu(z)$	Conley et al. (2011)
Data set extension I			
ISW-density cross	*WMAP*3	C_l^{gT}	Ho et al. (2008)
Velocity power spectrum	6dFGSv	$\mathcal{P}_{vv}(k)$	Johnson et al. (2014)
BAO (reconstructed)[a]	WiggleZ	$D_V(r_s^{\rm fid}/r_s)$	Kazin et al. (2014)
....	DR11 CMASS	$D_A(z)(r_s^{\rm fid}/r_s), H(z)(r_s/r_s^{\rm fid})$	Anderson et al. (2014b)
Power spectrum multipoles	DR11 CMASS	$P_0(k), P_2(k)$	Beutler et al. (2014)
....	WiggleZ ($z_{\rm eff} = 0.44$)	$P_0(k), P_2(k), P_4(k)$	Blake et al. (2011a)[b]
....	WiggleZ ($z_{\rm eff} = 0.73$)	$P_0(k), P_2(k), P_4(k)$	Blake et al. (2011a)[b]
Data set extension II			
RSDs	6dFGS	$f\sigma_8(z)$	Beutler et al. (2012)
RSD-BAO-AP	WiggleZ	$A(z), F_{AP}(z), f\sigma_8(z)$	Blake et al. (2012)
RSD-BAO-AP	BOSS CMASS	$D_V/r_s(z), F_{AP}(z), f\sigma_8(z)$	Beutler et al. (2014)

Notes. [a]Both the reconstructed BAO measurements (CMASS and WiggleZ) have been calculated by marginalizing over the general shape of the correlation function. Marginalizing over the shape decorrelates the BAO measurement with the power-spectrum multipole measurement, allowing one to fit for both measurements simultaneously.
[b]Note, however, these measurement have been updated in this work using an improved methodology.

and,

$$G(z_i, z_j)$$

$$\equiv \left(\frac{5}{\ln 10}\right)^2 \left(1 - \frac{(1+z_i)^2}{H(z_i)D_L(z_i)}\right) \left(1 - \frac{(1+z_j)^2}{H(z_j)D_L(z_j)}\right),$$

where $\alpha_{ij} = \cos^{-1}(\hat{r}_i \cdot \hat{r}_j)$, $A_{ij} \equiv |\boldsymbol{r}_i - \boldsymbol{r}_j|$ and $\boldsymbol{r}_i$ is the position vector of the ith galaxy. This analytic solution for the window function was presented by Ma, Gordon & Feldman (2011). For further details on this calculation we refer the reader to Johnson et al. (2014).

For this analysis, we perform a full likelihood calculation using the 6dFGSv PV sample. This is done using the covariance matrix (equation 10). The velocities in this sample are derived by Springob et al. (2014) using the Fundamental Plane (FP) relation. To calculate the covariance matrix, we integrate over the wavenumber range $k = 0.0005$–$0.15\,h\,{\rm Mpc}^{-1}$. For this calculation, we neglect velocity bias because large-scale information currently dominates in PV measurements.

Joachimi, Singh & Mandelbaum (2015) recently reported a detection of spatial correlations among offsets in galaxy size from a FP. Moreover, they highlight that this trend will bias measurements of the velocity power spectra at the 10 per cent level for $k > 0.04\,{\rm Mpc}^{-1}$. In relation to this potential source of systematic bias, we note that Johnson et al. (2014) demonstrated that the velocity power-spectra measurements were consistent when using PVs derived from different distance indicators; as such, we argue that *currently* this trend does not significantly influence our results.

In order to minimize the influence of poorly understood non-linear effects a non-linear velocity dispersion component $\sigma_{\rm PV}$ is introduced into the diagonal elements of the covariance matrix (Silberman et al. 2001). This nuisance parameter is marginalized over

in the analysis. The covariance matrix is thereby updated:

$$\Sigma_{ij} \equiv C_{ij}^{\rm m} + \sigma_{\rm PV}^2 \delta_{ij} . \tag{11}$$

One can now define the posterior distribution as z

$$P(\Sigma|\delta\boldsymbol{m}) = |2\pi\Sigma|^{-1/2} \exp\left(-\frac{1}{2}\delta m^{\rm T}\Sigma^{-1}\delta m\right), \tag{12}$$

where $\delta\boldsymbol{m}$ is a vector of the observed apparent magnitude fluctuations. Note the dependence on the cosmological model is introduced through the covariance matrix.

The model velocity power spectrum is generated using a transfer function. This can be defined starting from the PV in the synchronous gauge $v_p^{(s)}$ (cf. Ma & Bertschinger 1995).[1] As this gauge is defined in the dark matter rest frame, i.e. there are no temporal g_{00} perturbations, a gauge transformation is necessary. Using the convention of Ma & Bertschinger (1995), we define h and η as the metric perturbation in the synchronous gauge. Now by moving into the Newtonian gauge one finds the appropriate transfer function:

$$T_v(k) = \frac{c}{k^2}\left(k\alpha + \rho_b\, v_p^{(s)}/(\rho_b + \rho_c)\right), \tag{13}$$

where $k^2\alpha = \dot{h}/2 + 3\eta$.

In Fig. 1, we plot the measurements of $\mathcal{P}_{vv}(k)$ by Johnson et al. (2014), here the blue (green) points were measured using the 6dFGSv (low-z SNe) sample. For this plot the black line shows the power-spectrum prediction assuming GR, while the red and orange lines show the predictions for different values of the post-GR parameters. For these calculations the *Planck* best-fitting parameters are assumed. Additionally, the green line shows the prediction when using our best-fitting parameter values (see Section 5 for details).

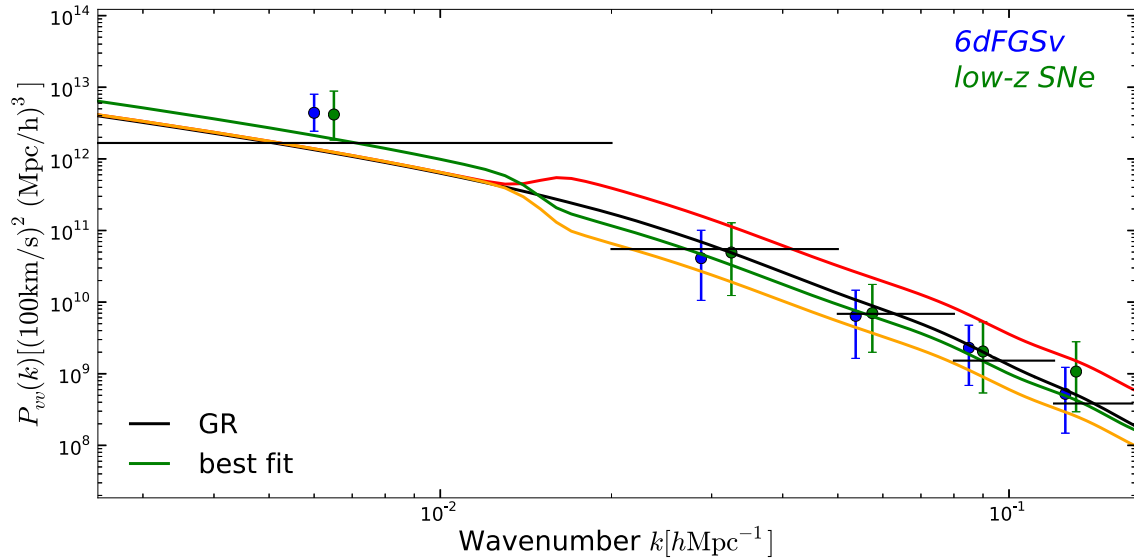[1] Our starting point is set by variables used within CAMB.

Figure 1. The velocity power-spectrum $\mathcal{P}_{vv}(k)$ at $z = 0$ for different parameter combinations of the adopted phenomenological model. The black line shows the prediction assuming General Relativity, and the orange and red lines illustrate the effect of varying the low-z and high-k bin for G_{matter}. For the red line $G_{matter}(z < 1; k > 0.01) = 1.8$ and for the orange line $G_{matter}(z < 1; k > 0.01) = 0.3$: for these predictions the standard cosmological parameters are fixed at the *Planck* best-fitting values, and unless specified otherwise all non-GR parameters are set to be consistent with GR (i.e. set equal to 1). Moreover, the green line shows the prediction found using the best-fitting parameter values found using set 4 (see Section 5 for details). The best-fitting values here correspond to the parameter values that maximize the likelihood. The blue and green data points correspond to the 68 per cent confidence intervals for the mean power within each bin for the 6dFGSv data and the low-z SNe data set constructed in Johnson et al. (2014). The thick black line indicates the mean power predicted by GR in each k-bin, this is calculated assuming a *Planck* cosmology.

Note the time evolution of the density perturbation Δ_m is set by a friction term $2\mathcal{H}\Delta_m$ and a source term $k^2\psi$. Therefore, by modifying G_{matter} one changes the source term to $k^2\psi \sim a^2 G_{matter}(k, z)\Delta_m$; hence, with $G_{matter}(k, z) > 1$ both the late-time clustering and the amplitude of the velocity power spectrum are enhanced.

3.2 Power-spectrum multipoles

We measured the multipole power spectra of the WiggleZ Survey data using the direct estimation method introduced by Yamamoto et al. (2006) and extended by Blake et al. (2011a) and Beutler et al. (2014). We provide a brief summary of the technique here, referring the reader to the above papers for a full description.

The redshift–space 2D galaxy power-spectrum $P_g^s(k, \mu)$, where μ is the cosine of the angle of the wavevector $\mathbf{k}$ with respect to the line of sight, may be expressed in terms of multipole moments $P_\ell(k)$ using a basis of Legendre polynomials $L_\ell(\mu)$:

$$P_g^s(k, \mu) = \sum_{\text{even } \ell} P_\ell(k) L_\ell(\mu), \tag{14}$$

where

$$P_\ell(k) = \frac{2\ell + 1}{2} \int_{-1}^{1} d\mu \, P_g^s(k, \mu) L_\ell(\mu). \tag{15}$$

The power-spectrum multipoles provide a form of data compression; in linear theory all the information is contained in the $\ell = 0$, 2, 4 terms, with the first two multipoles dominating the observed signal.

The rapid estimation technique of using Fast Fourier Transform (FFT) methods to measure $P_g^s(k, \mu)$ in bins of k and μ, where μ is defined with respect to a fixed axis parallel to the line of sight of the field centre, and then estimating $P_\ell(k)$ by a direct sum over the binned results using equation (15), has two difficulties. First, for a wide-area survey the line-of-sight direction with respect

to which μ should be measured will not be fixed. Secondly, at low k the sum over μ bins is problematic to evaluate due to the limited number of modes available in Fourier space. The Yamamoto et al. (2006) method estimates $P_\ell(k)$ using a sum over all galaxies for each wavevector $\mathbf{k}$ on the FFT grid, allowing the line-of-sight vector to vary for each object and without binning in μ. Window function effects are included using a similar sum over unclustered objects. Additive corrections are included for shot noise and for the discreteness of the grid. The measurements are then binned by wavenumber $k = |\mathbf{k}|$.

Following the analysis of the WiggleZ baryon acoustic oscillations (Blake et al. 2011b), we estimated the $\ell = 0, 2, 4$ multipole power spectra in the (9, 11, 15, 22, 1, 3) h survey regions in the overlapping redshift ranges $0.2 < z < 0.6$, $0.4 < z < 0.8$, and $0.6 < z < 1.0$. We measured the spectra in 14 wavenumber bins of width $\Delta k = 0.02 \, h \, \text{Mpc}^{-1}$ in the range $0.02 < k < 0.3 \, h \, \text{Mpc}^{-1}$. For this analysis, however, we only use the non-overlapping redshift ranges that we label low-z and high-z. The results for the monopole and quadrupole are given in Fig. 2.

We determined the covariance matrix of each vector $[P_0(k), P_2(k), P_4(k)]$ by repeating the measurements in each survey region for a series of 600 mock catalogues, built from N-body simulations generated by the method of COmoving Lagrangian Acceleration (Tassev, Zaldarriaga & Eisenstein 2013). As described by Kazin et al. (2014), we produced a halo catalogue by applying a friends-of-friends algorithm to the dark matter particles, and populated the haloes with mock galaxies using a Halo Occupation Distribution such that the projected clustering matched that of the WiggleZ galaxies. The mocks were sub-sampled using the selection function of each region, and galaxy co-ordinates converted to redshift–space.

We also determined the convolution matrix for each region and redshift slice, which should be used to project a model multipole vector to form a comparison with the data given the survey window
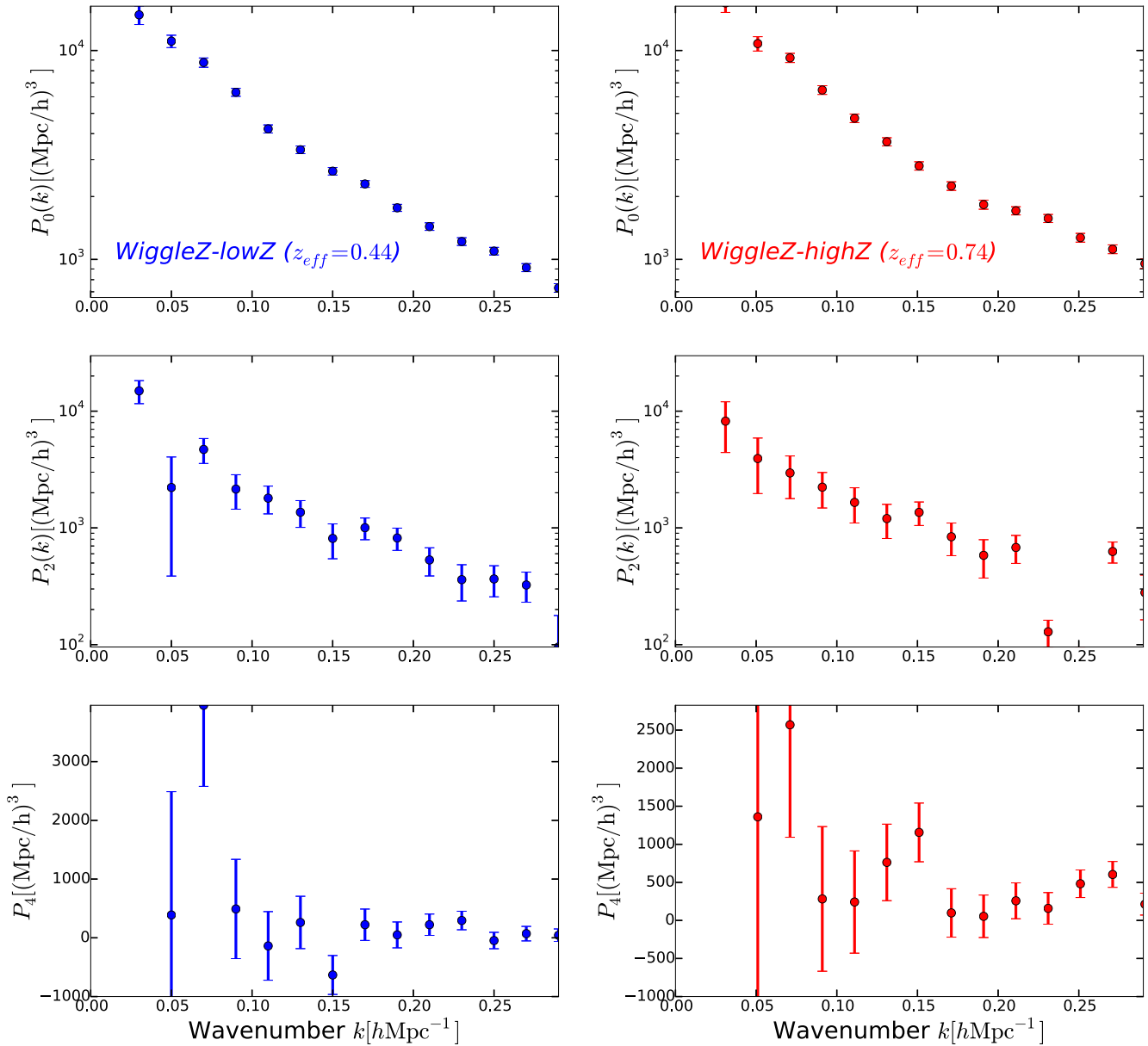
Figure 2. The monopole, quadrupole, and hexadecapole measurements from the WiggleZ survey, for both the high-z and low-z samples ($z = 0.44, 0.73$, respectively). For simplicity we combine the results from the six different survey regions; however, note this is not the format of the data we use, each survey region has a different window function and therefore is analysed separately.

function. For a wide-angle survey such as the Baryon Oscillation Spectroscopic Survey (BOSS), determination of the convolution involves a numerically intensive double sum over randomly distributed objects (Beutler et al. 2014). However, for the more compact WiggleZ Survey geometry, we found that it was acceptable (in the sense that any offset was far smaller than the statistical error) to use a flat-sky approximation, in which FFT methods were used to convolve a series of unit multipole vectors, generating each row of the convolution matrix in turn.

In addition to the WiggleZ multipole measurements, we include the monopole and quadrupole measurements from the BOSS-DR11 CMASS sample presented in Beutler et al. (2014); the reader is referred to this paper for technical details on the calculation. From the CMASS sample the $l = 0, 2$ multipole power spectrum are calculated for the wavenumber range $k = 0.01$–$0.20\,h\,\mathrm{Mpc}^{-1}$ with

a spacing of $\Delta k = 5 \times 10^{-3}\,h\,\mathrm{Mpc}^{-1}$. These measurement are presented for both the North and South Galactic Cap regions at an effective redshift of $z_{\mathrm{eff}} = 0.57$.

We plot the CMASS multipole measurements in Fig. 3. For this plot the blue-dashed (red-dashed) lines show the multipole predictions when setting $G_{\mathrm{matter}}(k > 0.01; z < 1) = 1.8$ ($G_{\mathrm{matter}}(k > 0.01; z < 1) = 0.3$), while the black lines show the prediction assuming GR. For these predictions the best-fitting parameters from *Planck* are assumed, in addition we set the bias to $b = 1.85$, the non-Poisson contribution to shot noise to $N = 1800\,h^{-3}\,\mathrm{Mpc}^3$, and the velocity dispersion to $\sigma_v = 4\,h^{-1}\,\mathrm{Mpc}$. Moreover, the orange lines give the prediction when using our best-fitting model parameters (see Section 5 for details). Note, for simplicity the theory predictions have only been convolved with the North Galactic Cap (NGC) window function.
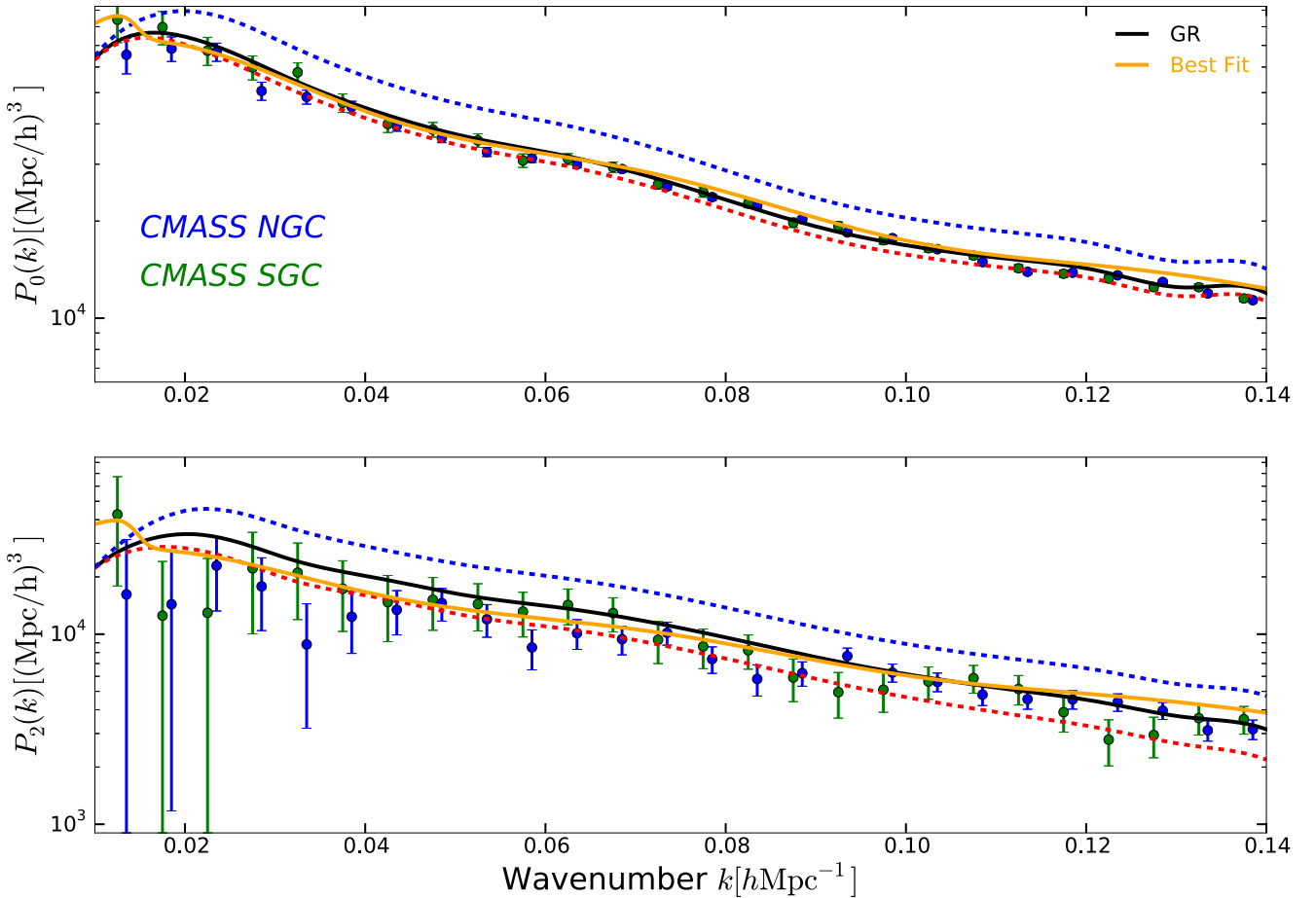
Figure 3. The monopole and quadrupole power spectrum for both the BOSS-DR11 CMASS survey regions (NGC and SGC). The blue-dashed line shows the prediction with $G_{matter}(k > 0.01; z > 1) = 1.8$, the red-dashed lines $G_{matter}(k > 0.01; z < 1) = 0.3$; for these predictions the best-fitting parameters from *Planck* are assumed and we set the bias to $b = 1.85$, the non-Poisson contributions to the shot noise to $N = 1800 \, h^{-3} \, \mathrm{Mpc}^3$, and the velocity dispersion to $\sigma_v = 4 \, h^{-1}$ Mpc. In this plot, for simplicity, the theory predictions have only been convolved with the NGC window function. The orange lines gives the prediction from the best-fitting model parameters (see Section 5 for details), convolved with the NGC window function. Note, for the final analysis we only fit our model to $k_{max} = 0.10 \, h \, \mathrm{Mpc}^{-1}$.

3.2.1 Modelling the power-spectrum multipoles

To model the redshift–space 2D galaxy power-spectrum $P_g^s(k, \mu)$ we use linear theory plus an empirical Gaussian damping term (Hatton & Cole 1998); the resulting model is given by

$$P_g^s(k, \mu) = \left[P_{gg}(k) - 2\mu^2 P_{g\theta}(k) + \mu^4 P_{\theta\theta}(k) \right] D(\mu, k) , \qquad (16)$$

where $D(\mu, k) = \exp \left[-(kf\mu\sigma_v)^2 \right]$. The standard interpretation of this damping, which is clearly observed in redshift surveys, is the uncorrelated pairwise velocity dispersion of galaxies. We absorb our ignorance by treating σ_v as a free parameter to be marginalized over for each survey.

Assuming linear theory the continuity equation (equation 3) can be written in Fourier space as

$$\theta(k) = -f(a)\delta(k) . \qquad (17)$$

However, we are modifying the gravitational field equations, so one needs to be self-consistent, given that the modifications (equation 7) will change the growth rate in a scale-dependent manner. We calculate this modified scale-dependent growth rate as

$$f(k, a) = \frac{d \ln \Delta_c(k, a)}{d \ln a} . \qquad (18)$$

This is self-consistent given CAMB contains all the relevant physics, i.e. the density and velocity variables are evolved according to the modified field equations. As a reminder of the potential scale-dependence we write the growth rate as $f(k)$. Note, for both the CMASS and WiggleZ multipoles the standard Poisson shot noise $(1/\bar{n})$ has been subtracted. However, for the CMASS multipoles (reflecting the approach taken by Beutler et al. 2014) we include a free parameter N to account for non-Poisson contributions to the shot noise (Baldauf et al. 2013). Now assuming a local, scale-independent linear bias ($\delta_g = b\delta$) and no velocity bias ($\theta_g = \theta$) equation (16) reduces to

$$P_g^s(k, \mu) = b^2 \left(P_{\delta\delta}(k) + N \right) \left(1 + f(k)\mu^2/b \right)^2 D(\mu, k). \qquad (19)$$

To justify the previous assumptions we truncate the fit for both the WiggleZ and CMASS multipoles to relatively large scales; to wit, we set $k_{max}^{CMASS} = 0.10 \, h \, \mathrm{Mpc}^{-1}$ and $k_{max}^{WiggleZ} = 0.15 \, h \, \mathrm{Mpc}^{-1}$. The WiggleZ measurements are used to a higher wavenumber because of the smaller bias of the sample ($b \sim 1$), in addition to the larger error bars.[2] The satellite fraction of the sample will also influence

---

[2] With a lower biased tracer, for example, the effect of non-local halo bias is less significant (Chan, Scoccimarro & Sheth 2012).

the wavenumber at which non-linear (one-halo) contributions are significant. On this point, we note that Halo Occupation Distribution fits to the projected clustering of WiggleZ galaxies (Koda et al. 2015) show that WiggleZ galaxies have a satellite fraction consistent with zero, and the projected clustering can be produced by central galaxies alone.

The matter power spectrum is calculated within CAMB using only linear theory: we choose not to incorporate non-linear corrections via HALOFIT. The use of HALOFIT presents an issue as the corrections have not been shown to be valid for general MG models.

In order to correctly interpret RSD measurements one is required to consistently incorporate our ignorance of the expansion history of the universe (viz., $H(z)$), bearing in mind that these measurements are performed assuming a fiducial cosmological model. As a result, in a trial cosmology, the growth-rate measurements should be adapted using the covariance with the Alcock–Paczynski (AP) distortion. Any discrepancy between the chosen fiducial expansion history ($\hat{D}_A(z)$, $\hat{H}(z)$) and the physical expansion history ($D_A(z)$, $H(z)$) can be accounted for by scaling the true (physical) radial and tangential wavenumbers ($k_\parallel^{\text{true}}$, $k_\perp^{\text{true}}$). The amplitude of the wavenumber scalings is determined by

$$\alpha_\parallel = \frac{H^{\text{fid}}(z)}{H(z)}, \quad \alpha_\perp = \frac{D_A(z)}{D_A^{\text{fid}}(z)}. \tag{20}$$

Hence the observed wavenumbers are given by $k_\parallel^{\text{obs}} = \alpha_\parallel k_\parallel^{\text{true}}$, and $k_\perp^{\text{obs}} = \alpha_\perp k_\perp^{\text{true}}$. Including this scaling in equation (19) one finds (Ballinger, Peacock & Heavens 1996; Matsubara & Suto 1996; Simpson & Peacock 2010)

$$P_g^s(k', \mu') = \frac{b^2}{\alpha_\perp^2 \alpha_\parallel} \left[1 + \mu'^2 \left(\frac{1+\beta}{\alpha_\parallel^2/\alpha_\perp^2} - 1 \right) \right]^2$$
$$\times \left[1 + \mu'^2 \left(\frac{\alpha_\perp^2}{\alpha_\parallel^2} - 1 \right) \right]^{-2}$$
$$\times P_{\delta\delta} \left[\frac{k'}{f_\perp} \sqrt{1 + \mu'^2 \left(\frac{\alpha_\perp^2}{\alpha_\parallel^2} - 1 \right)} \right] \times D(\mu, k), \tag{21}$$

where $k' = \sqrt{(k_\perp^{\text{obs}})^2 + (k_\parallel^{\text{obs}})^2}$, $\mu' = k_\parallel^{\text{obs}}/k'$, and $\beta = f/b$. This scaling introduces a new source of anisotropy in the clustering of galaxies, making it partially degenerate with RSD effects, accordingly it is important to account for this effect in this type of analysis (Blake et al. 2012; Beutler et al. 2014).

Two components must be included to compare our theoretical predictions with observations: the window function and integral constraint effect, both of which result in a distortion to the measured power spectrum relative to the true power spectrum. Window function effects are induced by the complex geometry of the survey (viz., a non-cubical geometry); and the integral constraint effect occurs as the condition $\delta_{k=0} = 0$ is applied to the data: this imposed normalization for the $k = 0$ mode is invalidated by supersurvey modes. Both effects induce a suppression of power at low-k (Peacock & Nicholson 1991; Beutler et al. 2014).

A consistent comparison between our model and the observations therefore requires us to include the window function effects in our modelling. Following Beutler et al. (2014) the convolved multipoles $P_l^{\text{conv}}(k)$ are calculated for the CMASS sample as

$$P_\ell^{\text{conv}}(k) = 2\pi \int dk' k'^2 \sum_L P_L^{\text{theory}}(k') |W(k, k')|_{\ell L}^2 - P_l^{ic}(k), \tag{22}$$

where

$$\left| W(k, k') \right|_{\ell L}^2 = 2i^\ell (-i)^L (2\ell+1) \sum_{ij, i \neq j}^{N_{\text{ran}}} w_{\text{FKP}}(\boldsymbol{x}_i) w_{\text{FKP}}(\boldsymbol{x}_j)$$
$$j_\ell(k|\Delta\boldsymbol{x}|) j_L(k'|\Delta\boldsymbol{x}|) \mathcal{L}_\ell(\hat{\boldsymbol{x}}_h \cdot \Delta\hat{\boldsymbol{x}}) \mathcal{L}_L(\hat{\boldsymbol{x}}_h \cdot \Delta\hat{\boldsymbol{x}}),$$

and the integral constraint term is given by

$$P_\ell^{\text{ic}}(k) = 2\pi \frac{|W(k)|_\ell^2}{|W(0)|_0^2} \int dk' k'^2 \sum_L P_L^{\text{theory}}(k') |W(k')|_L^2 \frac{2}{2L+1}.$$

Here j_L are spherical Bessel functions of order L, N_{ran} is the number of galaxies in the synthetic catalogue, and we sum over the monopole and quadrupole ($L = 0, 2$).

Each survey region has a different window function and hence needs to be treated separately. To compute the CMASS likelihood we use the publicly available CMASS window functions.[3] For example, the WiggleZ likelihood is computed as

$$-2\ln\left(\mathcal{L}^{\text{WiggleZ}}\right)$$
$$= \sum_{i=1}^{12} (\boldsymbol{P}_i^{\text{WiggleZ}} - \boldsymbol{P}_i^{\text{Conv}})^{\text{T}} \hat{C}_{\text{Wig},i}^{-1} (\boldsymbol{P}_i^{\text{WiggleZ}} - \boldsymbol{P}_i^{\text{Conv}}).$$

The i indices specify the two redshift bins and six survey regions for WiggleZ, and $\boldsymbol{P}_i^{\text{conv}} = [P_0^{\text{conv}}(k), P_2^{\text{conv}}(k), P_4^{\text{conv}}(k)]_i$. The hat in on the covariance matrix indicates that we are using a statistical estimator for the inverse covariance matrix. This estimator is determined by the covariance matrix measured from mock catalogues: typically one would use $\hat{C}^{-1} = C_{\text{mock}}^{-1}$, however, the noise in the derived covariance matrix (C_{mock}^{-1}) makes this estimator biased (Hartlap, Simon & Schneider 2007). We correct this bias using the estimator[4]

$$\hat{C}^{-1} = \frac{N_s - n_b - 2}{N_s - 1} C_{\text{mock}}^{-1}, \tag{23}$$

where n_b is the number of power-spectrum bins, and N_s the number of mock realizations used to construct the covariance matrix.

3.3 BAOs

Acoustic oscillations in the photon–baryon plasma, prior to recombination, imprint a series of fluctuations in large-scale structure: in configuration-space one finds a preference for galaxies to be distributed with a given comoving separation ($\sim$105 h^{-1} Mpc).

This excess in clustering (the BAO feature) functions as a cosmic yard-stick allowing the cosmic expansion history to be mapped out. By measuring the spherically averaged BAO position one determines

$$D_V(z) = \left[cz(1+z)^2 D_A(z)^2 / H(z) \right]^{1/3}. \tag{24}$$

Here $D_A(z)$ is the angular diameter distance. With higher signal-to-noise measurements one can extract more information by isolating the transverse and line-of-sight BAO positions, determining

$$\alpha_{\text{perp}} = D_A(z) r_s^{\text{fid}} / D_A^{\text{fid}}(z) r_s \tag{25}$$

$$\alpha_{\text{par}} = H_{\text{fid}}(z) r_s^{\text{fid}} / H(z) r_s. \tag{26}$$

---

[3] https://sdss3.org/science/boss_publications.php
[4] Note, we neglect the secondary correction to this term introduced by Percival et al. (2014). We estimate the magnitude of this effect, which is an error-in-the-error, to be around 5 per cent.

By including the dependence on r_s (the sound horizon at the drag epoch), and expressing the measured quantity as a ratio of the fiducial prediction, the dependence on CMB physics and the assumed cosmology has been made explicit.

To constrain the expansion history we use the following BAO measurements: WiggleZ reconstructed from Kazin et al. (2014), reconstructed DR11–CMASS and DR11–LOWZ from Anderson et al. (2014b), and the 6dFGS measurement from Beutler et al. (2011). By 'reconstructed' we are referring to the process of sharpening the acoustic peak by using information from the local density field (cf. Padmanabhan et al. 2012). The above measurements (excluding CMASS) can be incorporated into a likelihood given by

$$-2\ln\mathcal{L} = (x - \mathcal{S})^T C^{-1} (x - \mathcal{S}), \quad (27)$$

with the theory vector

$$
\begin{aligned}
x = [&D_V(0.44)(r_{\text{fid}}/r_s), D_V(0.6)(r_{\text{fid}}/r_s), D_V(0.73)(r_{\text{fid}}/r_s) \\
&D_V(0.32)/r_d, r_s/D_V(0.106)],
\end{aligned}
\quad (28)
$$

the data vector

$$\mathcal{S} = [1716, 2221, 2516, 8.25, 0.336], \quad (29)$$

and the covariance matrix[5]

$$
C_{\text{BAO}}^{-1} =
\begin{pmatrix}
2.17898 & 1.11633 & 0.46982 & 0 & 0 \\
1.11633 & 1.70712 & 0.71847 & 0 & 0 \\
0.46982 & 0.71847 & 1.65283 & 0 & 0 \\
0 & 0 & 0 & 36.025 & 0 \\
0 & 0 & 0 & 0 & 4444.4
\end{pmatrix}.
$$

The CMASS measurements are in the form of probability distributions for $P(\alpha_{\text{perp}})$ and $P(\alpha_{\text{par}})$ evaluated at $z_{\text{eff}} = 0.57$. These measurements are therefore analysed separately, for details see Anderson et al. (2014b). A number of these BAO measurements have been calculated using the approximate fitting formula for $r_s(z_d)$ from Eisenstein & Hu (1998); hence throughout, where appropriate, the BAO measurements derived using this approximation are scaled to be consistent with the result from CAMB (cf. Mehta et al. 2012).

To further improve the redshift range of our expansion history measurements we extend this 'base' sample by including the Lyman α BAO measurement from Delubac et al. (2014), and the Quasar–Ly α cross-correlation measurement from Font-Ribera et al. (2014). The measurements are $D_H(z = 2.34)/r_s = 9.18 \pm 0.28$, $D_A(z = 2.34)/r_s = 11.28 \pm 0.65$, $D_H(z = 2.36)/r_s = 9.0 \pm 0.3$, $D_A(z = 2.36)/r_s = 10.8 \pm 0.4$, where $D_H = c/H$. Both common cosmic variance or a common source for the measurement error would induce correlations between the Lyman α measurement. Fortunately, the origin of the dominant error components for these measurements are distinct, and hence the measurements are uncorrelated (Font-Ribera et al. 2014). Additionally, we treat any correlations between the BOSS and WiggleZ surveys as insignificant, given the small overlapping area ($\sim$550 deg^2) and the significance of shot noise in WiggleZ measurements (Beutler et al. 2016).

3.4 Growth-rate and Alcock–Paczynski measurements

The growth-rate measurements presented in this section will be used to constrain γ. Following the arguments presented in

subsection 3.2.1 we only include growth-rate constraints that have consistently incorporated the AP effect. The exception to this point is for very low-redshift observations, which are effectively insensitive to changes in the expansion history.

In order to self-consistently express the degeneracy with the expansion history we chose to fit to joint 3D posterior distributions from AP, BAO, and RSD measurements: as opposed to marginalized 1D constraints on $f\sigma_8(z)$. The growth-rate measurements we utilize are measured from BOSS-DR11 survey, the WiggleZ Dark Energy Survey, and the 6dF Galaxy survey (Beutler et al. 2012, 2014; Blake et al. 2012). For the CMASS sample we use the data vector[6]

$$
\begin{aligned}
\mathcal{S}_{k_{\text{max}}=0.20}^{\text{BOSS}} &= [D_V(0.57)/r_s(z_d), F_{\text{AP}}(0.57), f(0.57)\sigma_8(0.57)] \\
&= [13.88, 0.683, 0.422],
\end{aligned}
\quad (30)
$$

where the AP effect translates into a geometric constraint on $F_{\text{AP}}(z) = (1 + z)D_A(z)H(z)/c$. And the corresponding symmetric covariance matrix is given by

$$
10^3 C_{k_{\text{max}}=0.20}^{\text{BOSS}} =
\begin{pmatrix}
36.400 & -2.0636 & -1.8398 \\
 & 1.0773 & 1.1755 \\
 & & 2.0438
\end{pmatrix}.
\quad (31)
$$

The WiggleZ survey measurements are performed within three overlapping, hence correlated, redshift bins at $z_{\text{eff}} = 0.44, 0.60, 0.73$. We first split the data vector into redshift bins, namely $\mathcal{S}_{k_{\text{max}}=0.30}^{\text{WiggleZ}} = (\mathcal{S}_{z_1}, \mathcal{S}_{z_2}, \mathcal{S}_{z_3})$. In each of these redshift bins Blake et al. (2012) measure the parameter combination

$$\mathcal{S}_{z_i} = [A(z_i), F_{\text{AP}}(z_i), f(z_i)\sigma_8(z_i)], \quad (32)$$

where $A(z)$, the acoustic parameter, is given by

$$A(z) \equiv \frac{100 D_V(z)\sqrt{\Omega_m h^2}}{cz}. \quad (33)$$

The measured values are now $\mathcal{S}_{z_1} = (0.474, 0.482, 0.413)$, $\mathcal{S}_{z_2} = (0.442, 0.650, 0.390)$, and $\mathcal{S}_{z_3} = (0.424, 0.865, 0.437)$. Table 2 in Blake et al. (2012) gives the full covariance matrix for $\mathcal{S}^{\text{WiggleZ}}$.

The final measurement we use is $f(0.067)\sigma_8(0.067) = 0.423 \pm 0.55$ from Beutler et al. (2012). As noted previously, the AP effect is not significant for this measurement given the low-redshift nature of the sample. All of the introduced measurements are now incorporated using the likelihood

$$-2\ln\mathcal{L} = (x - \mathcal{S})^T C^{-1} (x - \mathcal{S}), \quad (34)$$

here x, $\mathcal{S}$, and C are the appropriate theory vector, data vector, and covariance matrix. Note that BAO information is included in both Sections 3.3 and 3.4 and we do not double-count this information.

4 SECONDARY DATA SETS

A brief introduction and motivation is given for the additional data sets we use.

4.1 Type Ia SNe

Sample variance effectively imposes a minimum volume limit for BAO detection. Accordingly, large volumes and hence higher redshift observations are preferable. Type Ia SNe measurements do not have this restriction and hence can provide very accurate constraints

---

[5] We have scaled the WiggleZ elements for clarity; the true covariance matrix is obtained by scaling the WiggleZ elements by 10^{-4}: $C_{\text{BAO}(1,1)}^{\text{True}-1} = 2.17898 \times 10^{-4}$.

[6] This result is found fitting the power-spectrum multipoles to $k_{\text{max}} = 0.20$ $h\,\text{Mpc}^{-1}$.

Table 2. Cosmological parameters used in our analysis. For each we give the symbol, uniform prior range, value taken in the ΛCDM cosmology, and summary definition. The parameters with a specified prior range are treated as free parameters in the MCMC analysis, while the remaining parameters are fixed at their fiducial values. The first block contains the standard parameters present in the ΛCDM model, while the second and third contain the parameters introduced to allow modifications from General Relativity. Note a prior is included on the derived parameter H_0.

Parameter	Prior range	Baseline	Definition
$\omega_b \equiv \Omega_b h^2$	[0.005, 0.1]	–	Baryon density today
$\omega_c \equiv \Omega_c h^2$	[0.001, 0.99]	–	Cold dark matter density today
$100\theta_{MC}$	[0.5, 10.0]	–	$100 \times$ approximation to r_*/D_A
τ	[0.01, 0.8]	–	Thomson scattering optical depth due to reionization
n_s	[0.9, 1.1]	–	Scalar spectrum power-law index ($k_0 = 0.05$ Mpc^{-1})
$\ln(10^{10}A_s)$	[2.7, 4.0]	–	log power of the primordial curvature perturbations ($k_0 = 0.05$ Mpc^{-1})
Ω_K		0	Curvature parameter today with $\Omega_{tot} = 1 - \Omega_K$
$\sum m_\nu$		0.06	The sum of neutrino masses in eV
N_{eff}		3.046	Effective number of relativistic degrees of freedom
Parameters model I			
z_t		1.0	Transition redshift for GR modifications
k_t		0.01	Transition wavenumber for GR modifications (Mpc^{-1})
$G_{light}(k, z)$	[−10, 10]	1	Modification to relativistic Poisson equation (equation 7)
$G_{matter}(k, z)$	[−10, 10]	1	Modification to non-relativistic Poisson equation (equation 7)
Parameters model II			
w_0	[−3.0, 1.0]	−1	Dark energy equation of state, $w(a) = w_0 + (1 - a)w_a$
w_a	[−3, 3]	0	Redshift-dependent modification to the equation of state (see above)
γ	[0, 2]	0.55	Power-law index of the structure growth-rate parameter $f(z) = \Omega_m^\gamma$
Ω_Λ		–	Dark energy density divided by the critical density today
Ω_m		–	Matter density (inc. massive neutrinos) today divided by the critical density
σ_8		–	RMS matter fluctuations today in linear theory
H_0	[20,100]	–	Current expansion rate in km s^{-1} Mpc^{-1}

on the low-redshift expansion rate: an epoch where the presence of 'dark energy' appears to dominate.

Therefore, we include the distance modulus measurements for 473 Type Ia SNe presented in Conley et al. (2011). The 'SNLS' sample is a combination of a number of previous surveys combining supernova legacy survey results with other low-z and high-z observations. These measurements are included in our analysis using the COSMOMC likelihood module provided by Conley et al. (2011).[7] This likelihood is evaluated by (first) calculating the model apparent magnitudes (or more accurately, the rest-frame peak B-band magnitude):

$$m_{model} = 5\log_{10}\mathcal{D}_L(z_{CMB}, z_{Hel}, \ldots) - \alpha(\mathcal{S} - 1) + \beta\mathcal{C} + \mathcal{M}_B.$$

Here $\mathcal{D}_L$ is luminosity distance with the dependence on the Hubble constant removed (it is dimensionless). And z_{CMB} and z_{Hel} are the CMB frame and heliocentric frame redshifts of the SN. $\mathcal{M}_B$ is a parameter which controls the zero-point and is a function of both the absolute magnitude of the SN and H_0, this parameter is marginalized over. The brightness of each SN is 'standardized' using observations of the shape of the light curve, s, and the colour $\mathcal{C}$; in addition to the empirical relationship of these parameter with the luminosity of the object: these dependences are characterized by the parameters α and β.

Writing the model predictions as a vector $\boldsymbol{m}_{model}$ the likelihood is given by

$$-2\ln\mathcal{L} = (\boldsymbol{m}_{obs} - \boldsymbol{m}_{model})^T C^{-1} (\boldsymbol{m}_{obs} - \boldsymbol{m}_{model}), \quad (35)$$

where $\boldsymbol{m}_{obs}$ is a vector of the observed B-band magnitudes. The elements of the non-diagonal covariance matrix C includes contributions from the following effects: the intrinsic-scatter of Type Ia

SN, the errors on the fitted light-curve parameters, the redshift error, a host correction error, and the covariance between s, $\mathcal{C}$, and m_{obs}. There are additional corrections for the local PV field, for further details see Conley et al. (2011).

In Section 5.5, we adopt a second SNe data set, namely the JLA sample (Betoule et al. 2014). This sample is composed of recalibrated SN Ia light curves and distances for the SDSS-II and SNLS samples; this sample can be distinguished from the SNLS sample by the treatment of systematic effects, the end result is a 1.8σ shift from the SNLS 3 yr results.

4.2 CMB

For the models we adopt GR is restored at the time of the last scattering surface; accordingly, the components of the temperature fluctuations, unmodified by large-scale structure, provide a powerful tool to both constrain the physical components of the universe and the initial conditions which seed large-scale structure.

The likelihood code for the power-spectrum C_l^{TT} from *Planck* is a hybrid: it is divided into high-l and low-l. For high-l ($l > 50$) we use the likelihood code CAMSPEC described by Planck Collaboration XV (2014b). This algorithm uses temperature maps derived at 100, 143, and 217 GHz. Once both diffuse Galactic emission and Galactic dust emission are masked, 57.8 per cent of the sky remains for the 100 GHz map and 37.3 per cent for the remaining maps. At low multipoles ($2 < l < 49$) the likelihood is computed using the Commander algorithm (Eriksen et al. 2008) using the frequency range 30–353 GHz over 91 per cent of the sky.

Sub-Hubble modes near reionization are damped by Thomson scattering, thus obscuring our view of the primordial power spectrum: we observe a fluctuation amplitude $A_s e^{-2\tau}$. The degeneracy between the optical depth τ and the amplitude of the primordial power-spectrum A_s can be partially broken by including

polarization data: the relative amplitude of the polarization and temperature power spectrum constrain τ. For this purpose we include the large-scale polarization measurements (C_l^{EE}) from *WMAP-9* (Bennett et al. 2013). We use the likelihood code from *Planck* which fits to the *l*-range ($2 < l < 32$).

4.2.1 CMB lensing

Photons travelling from the last scattering surface to our satellites encounter a number of over- and underdensities along the way. The intersected structure deflects the photon paths and the large-scale clustering of matter causes these deflection paths to be correlated over the sky (Blanchard & Schneider 1987). The combined effect of this CMB lensing is a re-mapping of the CMB temperature fluctuations (cf. Lewis & Challinor 2006):

$$T(\hat{\boldsymbol{n}}) = T^{\text{unlensed}}(\hat{n} + \nabla\Phi(\hat{\boldsymbol{n}})),\tag{36}$$

where $\Phi(\hat{\boldsymbol{n}})$ is the CMB lensing potential given by

$$\Phi(\hat{\boldsymbol{n}}) = -\int_0^{\chi^*} d\chi\, G(\chi, \chi^*)\left[\phi(\chi\hat{\boldsymbol{n}}; \eta_0 - \chi) + \psi(\chi\hat{\boldsymbol{n}}; \eta_0 - \chi)\right].$$
$$\tag{37}$$

Here χ is the conformal distance, η is the conformal time (η_0 is the time today), and $G(\chi, \chi^*)$ is a weighting function. The integration is taken from the last scattering surface (χ^*) to today ($\chi = 0$); hence this term represents the integrated effect of structure on photon paths, or more accurately, since we are interested in testing GR, the integrated effect of spatial and curvature perturbations.

The lensing power-spectrum $C_l^{\phi\phi}$ can be extracted from CMB maps; here we use the results from Planck Collaboration XVI (2014c) for the *l*-range $40 < l < 400$ (with the bin size $\Delta l = 64$): this *l*-range is chosen as it encompasses the majority of the lensing signal ($\sim$90 per cent) and is likely less influenced by systematic effects (cf. Planck Collaboration XVI 2014c). Given the lensing kernel peaks at $z \sim 2$ and we are only using $l < 400$, the lensing power-spectrum measurements used are only probing linear scales. Accordingly, we use linear theory to predict the lensing power spectrum and expect no systematic errors to be introduced from this modelling.

4.2.2 Temperature–galaxy cross-correlation

At late times the accelerating cosmic expansion dictates the evolution of density perturbations, one consequence is time-dependent metric potentials. This time-dependence is apparent in the CMB as it generates a net energy loss for CMB photons as they propagate through these potential wells (Sachs & Wolfe 1967). This feature is known as the ISW effect. The influence on the CMB power spectrum is given by

$$C_l \sim (\dot{\phi} + \dot{\psi}).\tag{38}$$

The ISW effect induces a correlation between the CMB (low-*l*) and large-scale structure probes: this is measured using the temperature–galaxy cross-correlation power-spectrum C_l^{gT} (cf. Ho et al. 2008). For our analysis we use the measurement of C_l^{gT} presented in Ho et al. (2008), and the likelihood code described in Dossett et al. (2011). This likelihood code expands on that presented in Ho et al. (2008) by including the effects of modified gravitational field equations.

The density field for the cross-correlation is approximated by the following measurements: the 2MASS Two Micron All Sky Survey, the Sloan-Digital Sky Survey Luminous Red Galaxy Sample,

the Sloan-Digital Sky Survey Quasars, and the National Radio Astronomy Observatory VLA Sky Survey. And the CMB temperature data is taken from *WMAP-5*.[8] The final *l*-range we adopt is $6 < l < 130$: this range is taken to ensure linear theory is valid, specifically, this *l*-range is imposed to ensure a wavenumber cutoff of $k \leq 0.05\ h\ \text{Mpc}^{-1}$.

5 MCMC ANALYSIS

We sample the parameter space of cosmological parameters using Markov Chain Monte Carlo techniques with the cosmomc package. The MCMC algorithm implemented within this code is an adaptive Metropolis–Hastings method which utilizes a number of techniques to ensure fast convergence times. The definitions and adopted priors of each parameter are given in Table 2. Our results are derived using eight separate chains which are run until convergence is achieved. The convergence of the Markov chains is determined using the Gelman and Rubin convergence criteria, for which chains require $R - 1 < 0.02$ to be satisfied for the least-converged orthogonalized parameter; R being the ratio of the variance of the chains' mean and the mean of the chains' variances (Gelman & Rubin 1992). The posterior mean and 68 per cent confidence intervals are then computed using thinned Markov chains.

There is currently no consensus on the H_0 value as measured from Cepheid data. The most up-to-date measurements are presented by Efstathiou (2014), Riess et al. (2011), and Humphreys et al. (2013): they measure $H_0 = 70.6 \pm 3.3, 73.8 \pm 2.4, 72.0 \pm 3\ \text{km s}^{-1}\ \text{Mpc}^{-1}$, respectively. Note both Efstathiou (2014) and Humphreys et al. (2013) have used the revised geometric maser distance to NGC 4258 (as presented in Humphreys et al. 2013), however their measurements still do not agree: the disagreement can be traced to different outlier rejection criteria being applied. For this analysis we adopt two approaches, because of this tension. When the expansion history is described by ΛCDM we do not include any H_0 prior as the model-dependent constraints from the CMB are sufficient. When we do include deviations from ΛCDM in the expansion history we add an H_0 prior using the measurement by Efstathiou (2014).

5.1 Parameter Fits: Model I

Using different combinations of the measurements outlined in the previous sections, we performed fits to the base ΛCDM parameters (ω_b, ω_c, θ_{MC}, τ, n_s, A_s) and the MG parameters $G_{\text{matter}}(k, z)$ and $G_{\text{light}}(k, z)$. Recall each MG parameter is binned in both redshift and scale.

In addition to the physical parameters, a number of nuisance parameters are introduced to account for unknown astrophysical effects. For the WiggleZ multipole calculation for each redshift bin we include the galaxy bias and velocity dispersion as nuisance parameters, that is, $b_{\text{lin}}(z = 0.44)$, $\sigma_v(z = 0.44)$, $b_{\text{lin}}(z = 0.73)$, and $\sigma_v(z = 0.73)$. The uniform priors imposed on these parameters are $b_{\text{lin}} \in [0.5, 3]$ and $\sigma_v \in [0, 10]\ h^{-1}$ Mpc. For the DR11-BOSS CMASS multipole measurement, we also include galaxy bias and velocity dispersion as free parameters, $b_{\text{lin}}(z = 0.57)$, $\sigma_v(z = 0.57)$.

---

[8] Note, the NVSS radio survey is the best tracer of large-scale structure at a high-redshift: this survey provides the most significant detection of a cross-correlation. Furthermore, the ISW effect is only dominant at low-*l* and hence is limited by cosmic variance. For both reasons, the measurement of C_l^{gT} has not been significantly improved from Ho et al. (2008), hence justifying our use of this data.

Table 3. The data set combinations we use for fits to Model I, in addition to the labels we adopt to refer to them. The corresponding data sets should be clear from the information given in Table 1. We define Base as the combination High$-l$ + low$-l$ + WP + BAO + SNe. Below CMASS refers to the monopole and quadrupole multipole measurements from the BOSS–CMASS sample. And WiggleZ refers to the monopole, quadrupole, and hexadecapole measurements from WiggleZ (as presented above).

Label	Description
SET 1	Base
SET 2	Base + Direct PV
SET 3	Base + CMASS ($k_{max} = 0.10\,h\,\mathrm{Mpc}^{-1}$)
	WiggleZ ($k = 0.15\,h\,\mathrm{Mpc}^{-1}$) + Direct PV
SET 4	Base + CMASS ($k_{max} = 0.10\,h\,\mathrm{Mpc}^{-1}$) +
	WiggleZ ($k = 0.15\,h\,\mathrm{Mpc}^{-1}$) + Direct PV
	+ ISW-Density + CMB Lensing
SET 5	Base + ISW-Density
SET 6	Base + CMASS ($k_{max} = 0.10\,h\,\mathrm{Mpc}^{-1}$)
SET 7	Base + CMASS ($k_{max} = 0.15\,h\,\mathrm{Mpc}^{-1}$)
SET 8	Base + WiggleZ ($k_{max} = 0.15\,h\,\mathrm{Mpc}^{-1}$)
SET 9	Base + WiggleZ ($k_{max} = 0.19\,h\,\mathrm{Mpc}^{-1}$)

Additionally for BOSS, we include a free parameter to account for the non-Poission contributions to shot noise N, this is given the prior ($N \in [0, 2000]\,h^{-3}\,\mathrm{Mpc}^3$).[9] For the velocity power-spectrum measurement, we include a velocity dispersion parameter $\sigma_{PV}(z = 0) \in [0, 500]\,\mathrm{km\,s}^{-1}$.

In order to understand the sensitivity of each cosmological probe to the physical parameters, and test for residual systematics, we analyse different combinations of cosmological probes. The different combinations are defined and labeled in Table 3 (henceforth we will use these definitions). The final results of this section are displayed in Figs 4 and 5, and further information is provided in Table 4. The first figure shows the constraints on $G_{matter}(k, z)$ and the second on $G_{light}(k, z)$. The black-dashed lines in both figures show the predictions from General Relativity. We do not plot the 2D contours between $G_{matter}(k, z)$ and $G_{light}(k, z)$ as their correlations are small, i.e. $\langle |\rho_c| \rangle \sim 0.15$. Here ρ_c is the cross-correlation coefficient, and $\langle \rangle$ indicates the average over all the possible values between $G_{matter}(k, z)$ and $G_{light}(k, z)$. Similarly, we do not plot the inferred constraints on the base ΛCDM parameters as, with two exceptions, the base ΛCDM parameters are not highly correlated with the post-GR parameters, the exception being σ_8 and Ω_m with G_{matter}. When averaging over the four G_{matter} parameters we find $\langle |\rho_c| \rangle \sim 0.77, 0.39$, respectively. The remainder of this section will involve a discussion of the content of these plots, in addition to some comments on potential systematics effects and the derived astrophysical parameters.

As shown in Fig. 4, we observe very little variation in $G_{light}(k, z)$ as we add extra data sets to the base sample (the green contour): this is because the ISW effect on the T–T power spectrum is dominating the fit; additionally, galaxy velocities have no sensitivity to $G_{light}(k, z)$, so we expect the benefit of including them

[9] We note that this shot noise contribution can potentially be negative (Baldauf et al. 2013), therefore one may question whether our imposed prior is overly constraining. However, we find that the posterior probability distribution for the CMASS shot noise parameter is well localized within the range of our chosen prior for all cases considered.
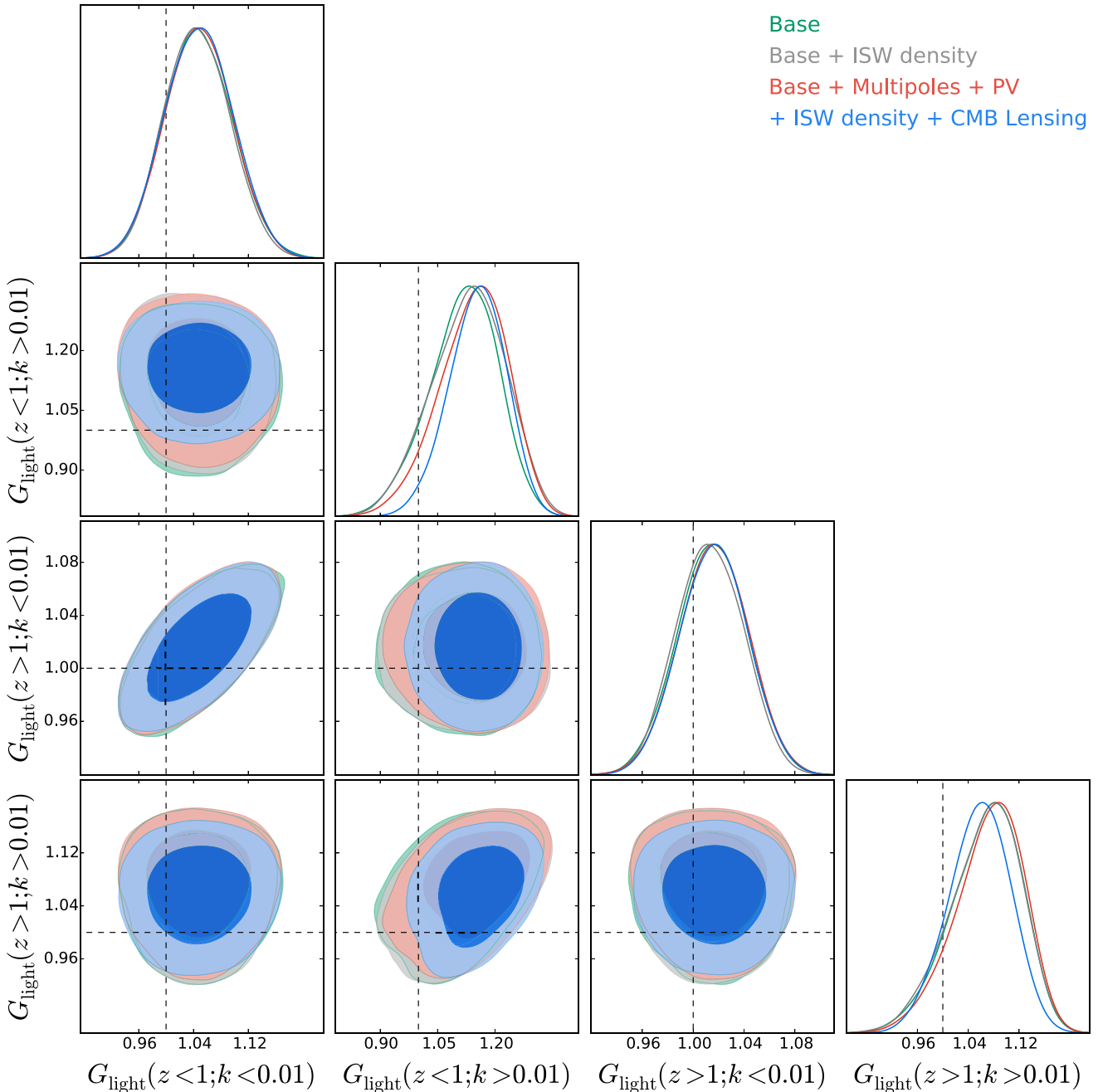
to be minimal. The grey contours in Fig. 4 are derived by adding the T–g measurements to the base sample, and the red contours are derived by adding the multipole and velocity measurements to the base sample. And the blue contours show the main results which are derived using Set 4. From these measurements for $G_{light}(k, z)$ we infer (in terms of 68 per cent CL)

$$G_{light}(z > 1; k > 0.01) = 1.057^{+0.053}_{-0.045},$$
$$G_{light}(z < 1; k < 0.01) = 1.048 \pm 0.048,$$
$$G_{light}(z < 1; k > 0.01) = 1.153^{+0.080}_{-0.068},$$
$$G_{light}(z > 1; k < 0.01) = 1.016 \pm 0.026.$$

These measurements are compatible at the 95 per cent CL with GR.

For $G_{matter}(k, z)$, we observe a significant amount of variation as new measurements are added to the base sample. In Fig. 5 the green, grey, red, and blue contours correspond, respectively, to measurements using the data set combinations Set 1, Set 2, Set 3, Set 4 (sets 6–9 are used for systematics checks to be discussed in the next section). As derived from Set 4 (i.e. using all the data sets) the 1D marginalized results for G_{matter} (in terms of 68 per cent CL) are

$$G_{matter}(z < 1; k > 0.01) = 0.65 \pm 0.43,$$
$$G_{matter}(z < 1; k < 0.01) = 1.22^{+0.39}_{-0.34},$$
$$G_{matter}(z > 1; k > 0.01) = 0.53 \pm 0.32,$$
$$G_{matter}(z > 1; k < 0.01) = 0.87 \pm 0.30.$$

Similarly to above, these results are consistent with GR at the 95 per cent CL, while at the 68 per cent CL level we observe a tension with GR in the high-redshift and large-wavenumber bin. Furthermore, the constraints from Set 4 on the 2D CL of the low-z high-k and high-z high-k bins of G_{matter} show a tension with the standard model at greater than 2σ. For the 1D marginalized results this tension is significantly reduced as the high-z and low-z G_{matter} bins are highly correlated, as can be seen in Fig. 5. This degeneracy occurs as some probes, such as the CMB, are sensitive to integrated quantities over redshift, such that higher growth at high-z can be compensated for by lower growth at low-z.

Introducing direct PV measurements the constraints shift from the green to the grey contours. The most prominent shift occurs in the low-z and low-k G_{matter} bin, as expected: we find a shift from $G_{matter}(z < 1; k < 0.01) = 0.81^{+0.59}_{-0.46}$ to $G_{matter}(z < 1; k < 0.01) = 1.32^{+0.42}_{-0.29}$. We find further improvements in the constraints for the high-wavenumber and low-redshift bin. Future PV surveys should be able to considerably improve on this situation (cf. Koda et al. 2014). Using the best-fitting parameters from Set 4, we measure $\chi^2_{6dFGSv} = 778$ with 979 data points: the full 6dFGSv velocity field is smoothed on to a grid with 979 non-empty elements (cf. Johnson et al. 2014).

Including RSD measurements results in the shift from the grey to red contours, for which we find a significant improvement in the constraint on the high-z and high-k G_{matter} bin. Moreover, we find that the RSD measurements have more influence on the high-z bin than the low-z bin: this is an further consequence of measuring integrated quantities. As a systematic check we isolate the measurements from WiggleZ and BOSS and perform separate fits, we find that the two separate constraints on G_{matter} are consistent. We can also assess how well our model fits the observations. By adding the multipole likelihoods we find $\Delta\chi^2 = 322$, for a total of 324 measurement points. Individually, for the fit to the WiggleZ multipoles, with 126 data points per redshift bin we measure $\chi^2_{WiggleZ} = 129.88$ for the low-z region, and $\chi^2_{WiggleZ} = 121.6$ for the high-z region.

Figure 4. 68 per cent and 95 per cent confidence regions for the four $G_{light}(k, z)$ bin parameters. Here, $z > 1$ is referring to the redshift range $2 > z > 1$. Note all of the parameters specified in Table 2 are being varied in this analysis, however for clarity we only plot the constraints on $G_{light}(k, z)$ in this plot. Recall we have defined Base as High$-l$ + low$-l$ + WP + BAO + SNe.

Finally, for BOSS, given we are fitting to $k_{max} = 0.10 \, h \, \text{Mpc}^{-1}$, there are 72 measurement points and we find $\chi^2_{CMASS} = 72.6$.

5.2 Model comparison: Bayesian evidence

To evaluate the statistical significance of deviations from GR we previously used the marginalized posterior distributions of G_{matter} and G_{light}. An alternative approach is to use model selection. This allows one to rank the viability of a series of models based on a measure (Jeffreys 1961). For cosmological applications see Liddle, Mukherjee & Parkinson (2006) and Trotta (2008). The philosophy

behind model selection is as follows: simple models with a high degree of predictability are favoured, equivalently, complex models with a large number of highly tuned parameters are penalized. The relevant measure weighs both the ability of the model to fit observations and its degree of simplicity.

To discriminate between models one first computes the evidence for each model, $\mathcal{E}$, which is defined as the probability of the data D given the model $\mathcal{M}$ (defined by a set of model parameters $\boldsymbol{\theta}$):

$$\mathcal{E} = P(D|\mathcal{M}) = \int P(D|\theta\mathcal{M})\pi(\theta|\mathcal{M}). \quad (39)$$
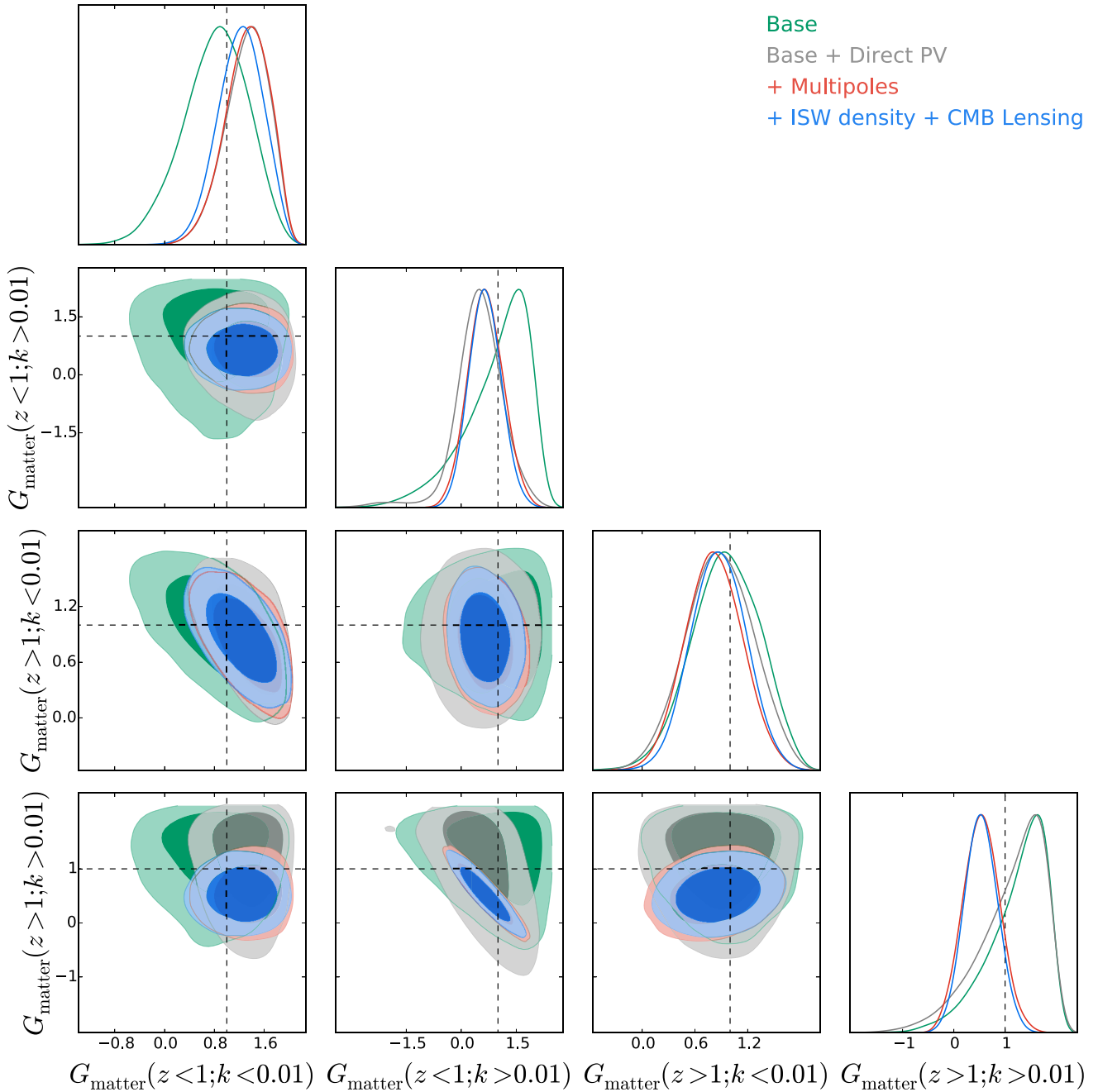
Figure 5. 68 per cent and 95 per cent confidence regions for the four $G_{\mathrm{matter}}(k, z)$ bin parameters. Here, $z > 1$ here is referring to the redshift range $2 > z > 1$. Note all of the parameters specified in Table 2 are being varied in this analysis yet for clarity we only plot the constraints on $G_{\mathrm{matter}}(k, z)$. Recall we have defined Base as High$-l$ + low$-l$ + WP + BAO + SNe.

In our case we will consider two models, $\mathcal{M}_1$ and $\mathcal{M}_2$, which represent GR and our phenomenological MG model, respectively. The ratio of the evidence values is called the Bayes factor, B, and the value of this indicates a degree of preference for one model over the other:

$$B_{12} = \frac{\int P(D|\theta_1 \mathcal{M}_1)\pi(\theta_1|\mathcal{M}_1)}{\int P(D|\theta_1 \mathcal{M}_2)\pi(\theta_1|\mathcal{M}_2)} . \tag{40}$$

One can extend this calculation by incorporating the posterior probabilities of the models by adding model priors of the form

$\pi(\mathcal{M})$. For our case, for simplicity we set $\pi(\mathcal{M}_1) = \pi(\mathcal{M}_2) = 1$. This choice suggests we have no preference (based on physical intuition) between the models.[10]

---

[10] Recent work by Gubitosi et al. (2015) suggest a method to incorporate the philosophical notion of falsifiability into model selection. This additional selection criteria arises when paradigms are being compared, and results in a more severe penalty for unfalsifiable paradigms. We will not include this additional selection effect here.

Table 4. Cosmological parameter constraints for Model I. The constraints are derived from four different groups of cosmological probes, we labels these groups Set 1 to 4 and define each in Table 3. For each parameter in each group we provide the 68 per cent confidence levels. To keep the table a reasonable size we only consider the parameters most relevant to our analysis.

Parameter	SET 1 68 per cent limits	SET 2 68 per cent limits	SET 3 68 per cent limits	SET 4 68 per cent limits
$G_{\text{matter}}(z < 1; k > 0.01)$	$0.96^{+1.1}_{-0.44}$	$0.48^{+0.59}_{-0.52}$	0.66 ± 0.47	0.65 ± 0.43
$G_{\text{matter}}(z < 1; k < 0.01)$	$0.81^{+0.59}_{-0.46}$	$1.32^{+0.42}_{-0.29}$	$1.32^{+0.41}_{-0.30}$	$1.22^{+0.39}_{-0.34}$
$G_{\text{matter}}(z > 1; k > 0.01)$	$1.23^{+0.71}_{-0.28}$	$1.12^{+0.81}_{-0.33}$	0.54 ± 0.35	0.53 ± 0.32
$G_{\text{matter}}(z > 1; k < 0.01)$	$0.95^{+0.42}_{-0.36}$	0.88 ± 0.37	0.82 ± 0.32	0.87 ± 0.30
$G_{\text{light}}(z > 1; k > 0.01)$	$1.067^{+0.063}_{-0.046}$	$1.066^{+0.064}_{-0.045}$	$1.072^{+0.063}_{-0.043}$	$1.057^{+0.053}_{-0.045}$
$G_{\text{light}}(z < 1; k < 0.01)$	1.048 ± 0.048	1.044 ± 0.050	1.048 ± 0.048	1.048 ± 0.048
$G_{\text{light}}(z < 1; k > 0.01)$	$1.12^{+0.10}_{-0.078}$	$1.113^{+0.098}_{-0.084}$	$1.14^{+0.10}_{-0.077}$	$1.153^{+0.080}_{-0.068}$
$G_{\text{light}}(z > 1; k < 0.01)$	1.015 ± 0.026	1.016 ± 0.027	1.016 ± 0.026	1.016 ± 0.026
$\Omega_b h^2$	0.02228 ± 0.00025	0.02227 ± 0.00025	0.02226 ± 0.00025	0.02230 ± 0.00025
$\Omega_c h^2$	0.1172 ± 0.0013	0.1172 ± 0.0013	0.1168 ± 0.0013	0.1163 ± 0.0013
τ	0.087 ± 0.013	$0.089^{+0.012}_{-0.014}$	0.089 ± 0.013	0.086 ± 0.012
$\ln(10^{10} A_s)$	3.076 ± 0.026	3.081 ± 0.025	3.080 ± 0.025	3.073 ± 0.025
Ω_Λ	0.7011 ± 0.0077	0.7009 ± 0.0078	0.7031 ± 0.0074	0.7060 ± 0.0074
Ω_m	0.2989 ± 0.0077	0.2991 ± 0.0078	0.2969 ± 0.0074	0.2940 ± 0.0074
σ_8	$0.851^{+0.14}_{-0.091}$	$0.783^{+0.095}_{-0.063}$	$0.717^{+0.018}_{-0.022}$	$0.711^{+0.017}_{-0.020}$
H_0	68.49 ± 0.61	68.46 ± 0.63	68.61 ± 0.59	68.83 ± 0.61

To compute the multidimensional integrals in equation (40) we use the software package MULTINEST, as presented by Feroz & Hobson (2008). This program uses the Monte Carlo technique importance nested sampling to compute the relevant integrals. For further details we refer the reader to Feroz & Hobson (2008). Moreover, for the results that follow, we adopt a conservative threshold for interpreting the bayes factor, specifically, we use the scale suggested by Kass & Raftery (1995).

Given evidence calculations are more computationally demanding than Markov chains, we do not include the velocity power spectrum likelihood in this calculation. Following the results above, we observe there is no strong tension between the velocity measurements and the ΛCDM model, hence we expect our conclusions (i.e. the evidence ratio) will not be sensitive to this likelihood. With the exclusion of the velocity likelihood, we use the remaining measurements, as introduced above.

For a ΛCDM cosmology we find a global log-evidence of $\ln(\mathcal{E}_{\Lambda\text{CDM}}) = -5423.75 \pm 0.15$. While allowing G_{matter} and G_{light} to vary we find, $\ln(\mathcal{E}_{\text{MG}}) = -5715.41 \pm 0.14$. Thus, we find an evidence ratio of $2\log(\mathcal{E}_{\text{MG}}/\mathcal{E}_{\Lambda\text{CDM}}) = -5.83 \times 10^2$. This ratio suggests 'strong evidence' in favour of the ΛCDM model. Or, equivalently, 'no support' for our phenomenological model. One can interpret this result as the extra parameters not significantly improving the fit to data, yet increasing the complexity of the model; accordingly, the model is strongly disfavoured.

For this calculation we include a theory prior on the parametrized deviations to GR. This prior ensures we only consider parameter combinations that produce positive C_ℓ's. We expect this prior to have a small impact on the final results for the following reasons. First, the posterior distributions are localized with the prior volume. And, secondly, reducing the prior volume with this theory prior one would improve the evidence towards the MG model. This model is already strongly disfavoured, hence any shift would not influence our conclusions. Had the MG model been favoured we would have been required to carefully consider the influence of this prior.

5.3 Checking systematics and astrophysical parameter constraints

When calculating the power-spectrum multipole predictions, we assumed a linear bias factor and linear perturbation theory. The validity of both assumptions may be questioned. We examine, albeit crudely, the importance of these assumptions by determining the sensitivity of the parameter fits to the small-scale cut-off k_{max}. For our model fits using the CMASS and WiggleZ multipole likelihood calculations we ran new Markov chains using different cut-off values $k_{\text{max}}^{\text{CMASS}} = 0.10, 0.15\, h\, \text{Mpc}^{-1}$ and $k_{\text{max}}^{\text{WiggleZ}} = 0.15, 0.19\, h\, \text{Mpc}^{-1}$. The results showed no statistically significant shift when the fitting range was changed. However, we emphasize that a detailed investigation of mock catalogues is needed to fully validate these assumptions.

The astrophysical parameters for the multipole and direct PV fits only vary slightly when using different data set combinations, hence we choose to only present results from Set 4 (given in terms of 68 per cent CL). For the fit to the WiggleZ multipole we find $\sigma_v(z = 0.73) = 2.30^{+1.2}_{-1.8}\, h^{-1}$ Mpc, $\sigma_v(z = 0.44) = 4.468^{+1.8}_{-1.0}\, h^{-1}$ Mpc, $b_1(z = 0.44) = 1.089 \pm 0.042$, and $b_1(z = 0.73) = 1.207 \pm 0.059$. For the fit to CMASS we find $\sigma_v(z = 0.57) = 2.44^{+0.68}_{-1.2}\, h^{-1}$ Mpc, $b_1(z = 0.57) = 2.055 \pm 0.084$, and $N(\text{Shot Noise}) = 705 \pm 200\, h^{-3}$ Mpc^3. Finally, from the fit to the velocity power spectrum we determine the 95 per cent upper limit $\sigma_{\text{PV}}(z = 0) < 334.6\, \text{km s}^{-1}$. With different k_{max} values adopted, one should not necessarily compare our results for the shot noise and velocity dispersion with previous analysis; however, we find our bias measurements to be consistent with previous analysis.

5.4 Previous measurements: summary and comparisons

Below we briefly summarize recent work in this field, with a focus on results that adopt a similar parametrization.

(i) Daniel & Linder (2010) presented constraints on $\{\mathcal{G}, V\}$, our $\{G_{\text{light}}, G_{\text{matter}}\}$, in bins of time and wavenumber. To constrain these

parameters they used the following probes: *WMAP*7, supernova Union2, CFHTLS weak-lensing data, temperature–galaxy cross-correlation, and the galaxy power spectrum. They identify the CFHTLS survey as responsible for a 2σ tension with GR in the high-k and low-z bin for $\mathcal{V}$. This feature is not observed when using the COSMOS data or in subsequent analysis of the final CFHTLenS catalogue (Heymans et al. 2012). Note RSD information was not included, therefore the final constraints on V are of the order of $\sim$1.

(ii) Simpson et al. (2013) measure the parameters $\{\Sigma, \mu\}$ (i.e. $\{G_{\mathrm{light}}, G_{\mathrm{matter}}\}$) using tomographic weak-lensing measurements from CFHTLenS and RSD measurements of $f\sigma_8$ from 6dFGS and WiggleZ, in addition to *WMAP*7 (including low-l) and geometric information (see also Dossett et al. 2015 and Zhao et al. 2012). Their measurements are consistent with GR: they find $\mu = 1.05 \pm 0.25$ and $\Sigma = 1.00 \pm 0.14$. For this fit they assumed Σ, μ are scale-independent and adopt a specific functional form for their temporal evolution: this effectively confines deviations to very low redshifts. Measurements of the T–g cross-correlations, CMB-lensing, and the growth-rate measurement from CMASS were not included in these fits.

(iii) Planck Collaboration XIII (2015) have recently provided the state-of-the-art measurements of post-GR parameters, placing constraints on an extensive range of specific and phenomenological models. For the phenomenological model they adopt the parameters $\{\mu, \eta\}$, as implemented in MGCAMB. Motivated by $f(R)$ models, a specific functional form for the redshift and scale dependence of these parameters is assumed. As appropriate to their aim, they ensure their angular cuts to the tomographic shear–shear measurements from CFHTLenS isolate the linear signal (see their fig. 2). This approach is not adopted throughout, however. Their adopted $f\sigma_8(z = 0.57)$ measurement (by Samushia et al. 2014) was derived by fitting the monopole and quadruple of the correlation function on scales larger than $25\,h^{-1}$ Mpc. As highlighted by the authors (see their fig. 7) non-linear terms are significant on these length-scales, the result is a dependence on non-linear physics.

In relation to the most up-to-date measurements, our results can be distinguished in two main ways: First, the inclusion of the velocity power-spectrum measurements, which improve low-k constraints; secondly, the methodology we use to analyse RSD measurements, and the range of RSD measurements analysed. We argue that the methodology of directly analysing the power-spectrum multipoles allows constraints to be derived that are more widely applicable to non-standard cosmological models. This is because it allows one to restrict the analysis to scales within the linear regime, where the phenomenological model we use describe physical models (see Section 1). Moreover, the multipoles contain scale-dependent information, which is necessary if scale-dependent terms are introduced.

5.5 Parameter fits: Model II

We now explore fits to a new parameter space that is more rigid regarding the allowed deviation to the growth history. Two scenarios will be considered when fitting for these parameters, first, an expansion history fixed to ΛCDM; and secondly, an expansion history than can deviate from ΛCDM via. a time-dependent equation of state. We define the two parameter spaces as $\boldsymbol{p}_1 = \{\gamma, \omega_{\mathrm{b}}, \omega_{\mathrm{c}}, \theta_{\mathrm{MC}}, \tau, n_{\mathrm{s}}, A_{\mathrm{s}}\}$, and $\boldsymbol{p}_2 = \{\gamma, w, w_a, \omega_{\mathrm{b}}, \omega_{\mathrm{c}}, \theta_{\mathrm{MC}}, \tau, n_{\mathrm{s}}, A_{\mathrm{s}}\}$. We choose not to include the influence that deviations in the expansion history have on the expected growth (that is, the relation $\gamma = f(\gamma_0, w_0, w_a)$) as the corrections are currently small.

Note that by changing the growth rate we modify σ_8, this effect is included by altering the growth history well into the matter dominated regime. The modified growth factor is calculated as

$$D(a_{\mathrm{eff}}) = \exp\left(-\int_{a_{\mathrm{eff}}}^{1} \mathrm{d}a\, \Omega_{\mathrm{m}}(a)^{0.55}/a\right),\qquad(41)$$

now we scale the fiducial prediction $\sigma_8^{\mathrm{Fid}}(z_{\mathrm{high}})$ to find the modified amplitude $\sigma_8^{\gamma}(z_{\mathrm{eff}})$:

$$\sigma_8^{\gamma}(z_{\mathrm{eff}}) = \frac{D(a_{\mathrm{eff}})}{D(a_{\mathrm{high}})}\sigma_8^{\mathrm{Fid}}(z_{\mathrm{high}}).\qquad(42)$$

The first set of results, which assume a ΛCDM expansion history are shown in Fig. 6. This plot shows the 68 per cent and 95 per cent 2D likelihood contours for the parameter combinations $\{\Omega_{\mathrm{m}}, \gamma\}$ and $\{\tau, \gamma\}$. The expected value of γ from GR is given by the grey-dashed line. In addition to the growth rate and AP constraints, these measurements are inferred using high-l + WMAP polarization (WP) + low-z BAO (which we label in this section as *base*). For fits in this section we do not use the low-l CMB T–T data or CMB lensing, since we have not included the dependence of these signals on γ. For the final constraint we measure $\gamma = 0.665 \pm 0.067$, which is consistent with GR at the 95 per cent CL.

The results for $\boldsymbol{p}_2$ are presented in Fig. 7, where we plot the 2D likelihood contours (68 per cent and 95 per cent), and the marginalized 1D probability distributions for $\gamma, w_0, w_a, \Omega_{\mathrm{m}}, \tau$. Again, the black-dashed lines indicate the values expected from the standard model; namely, $\gamma = 0.55$, $w_0 = -1$, and $w_a = 0$. The degraded constraint on γ is a direct result of the degeneracy between the expansion and growth histories: this is the reason we consider both a fixed and non-fixed expansion history.

We use four different data set combinations to constrain these parameters, they are defined as follows: fit 1 is the base sample, fit 2 is base + WP, fit 3 is base + WP + SNLS, and fit 4 is base + WP + JLA. We define base here as the combination High-l + H_0 + RSD/AP + low-z BAO. We use two SN samples in order to understand how sensitive the growth index is to our choice of adopted data set.

We will first discuss the main results, which are found using fit 3 and 4 (the red and blue contours in Fig. 7) and then consider how the constraints are influenced by the different probes. Using fit 3 we infer (in terms of 68 per cent CL) the marginalized constraints

$$w_0 = -0.98^{+0.13}_{-0.15},\qquad(43)$$

$$w_a = -0.42^{+0.62}_{-0.47},\qquad(44)$$

which are consistent with the standard model. In terms of deviation to the growth history we measure (in terms of 68 per cent CL)

$$\gamma = 0.76^{+0.089}_{-0.087}.\qquad(45)$$

This result is at tension with GR at a level greater than 2σ. Changing our SN sample to the JLA sample we find this tension is slightly reduced. Using fit 4 we now measure

$$\gamma = 0.73^{+0.08}_{-0.10},\qquad(46)$$

which is just consistent at the 2σ level, and for the expansion history we find $w_0 = -0.89^{+0.12}_{-0.12}$ and $w_a = -0.63^{+0.56}_{-0.45}$. Note, without including any SN data, using fit 2 (the grey contour in Fig. 7) we measure $\gamma = 0.69^{+0.09}_{-0.11}$, which is consistent at the 95 per cent CL. This may suggest there exists a mild tension between the growth rate and the SN measurements. Finally, we note our measurements of the growth index are relatively insensitive to the polarization
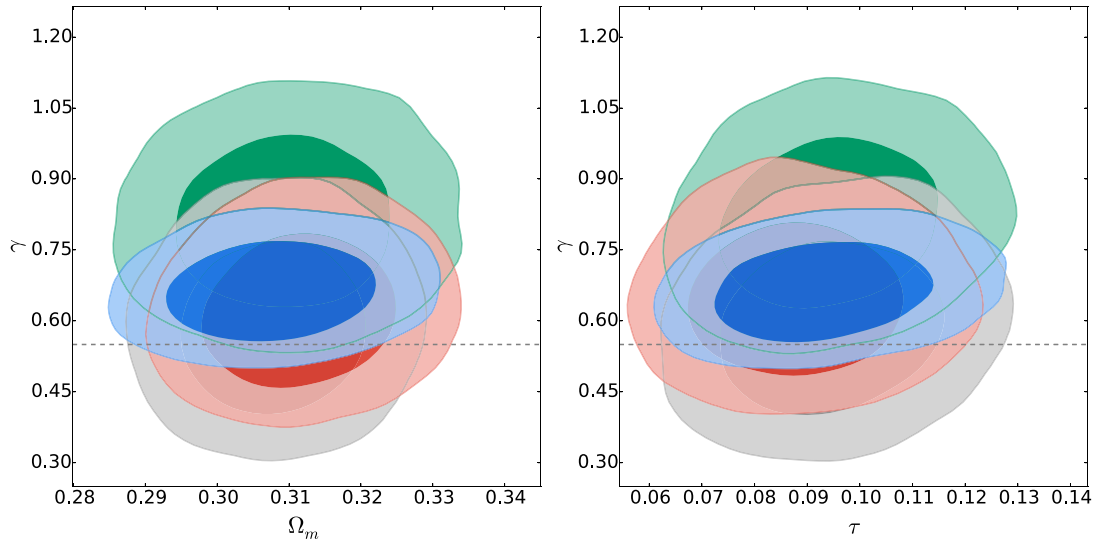
Figure 6. 2D marginalized posterior distributions for $\{\Omega_m, \gamma\}$ and $\{\tau, \gamma\}$, assuming a ΛCDM expansion history. The contours are the 68 per cent and 95 per cent CL. Below we refer to *base* as the data set combination high-l + WP + low-z BAO. The green contours are found using base + CMASS, the grey contours are found using base + WiggleZ, the red contours are founds using base + 6dFGS, and the blue contours show the combined fit to all the growth-rate measurements plus the base measurements. Moreover, we include the AP and BAO information with the growth-rate constraints, without double counting BAO measurements.

data, as can be observed in Fig. 7 by comparing the green (no WP) and grey (including WP) contours.

Comparing the best-fitting values for the expansion history using only BAO measurements with the BAO + SN fit (which is driven by SN) is interesting as it provides a test of the significance of non-linear structure on SNe distance measurements (Clarkson et al. 2012). With fit 2, which only uses the low-redshift BAO measurements to constrain the expansion history, we infer (in terms of 68 per cent CL) $w_0 = -0.68^{+0.29}_{-0.26}$ and $w_a = -1.27^{+0.92}_{-0.97}$. These measurements are consistent at the 95 per cent CL with the standard model and the constraints from the SN + BAO fit; moreover, they highlight the current necessity of Type Ia SN in placing tight constraints on the redshift evolution of the equation of state. By introducing the Lyman α BAO measurements into this fit we measure $w_0 = -0.58^{+0.27}_{-0.22}$ and $w_a = -1.55^{+0.74}_{-0.89}$, which indicates a tension with the standard model predictions at a level $>2\sigma$, in agreement with the results by Font-Ribera et al. (2014). Further checks for systematics will be required to confirm this result given its significance and the complexity of the measurement.

5.6 Comparison with previous results

Below we summarize a sub-sample of previous measurements of the parameters $\{w_0, w_a, \gamma\}$.

(i) Beutler et al. (2014) measure $\gamma = 0.772^{+0.124}_{-0.097}$ using the power-spectrum multipoles from the DR11 CMASS sample and *Planck*: this fit includes the AP effect, but does not allow for deviation in the expansion history. This value is consistent with the measurement by Sánchez et al. (2013) of $\gamma = 0.64 \pm 0.26$ found using the clustering wedges of CMASS combined with BAO and SNe measurements.

(ii) Rapetti et al. (2013) perform fits to $\{w_0, \gamma\}$ and γ. For a fixed expansion history, using *WMAP* combined with galaxy cluster data from *ROSAT* and *Chandra*, they measure $\gamma = 0.415^{+0.128}_{-0.126}$. When adding further data from RSD measurements (WiggleZ and 6dFGS) they find $\gamma = 0.570^{+0.064}_{-0.063}$.

(iii) Beutler et al. (2012) measure $\gamma = 0.547 \pm 0.088$ using *WMAP*7 and the two-point correlation function measured from 6dFGS. For this fit the expansion history is fixed, as the AP effect is not relevant. Note, there is a small difference between our measurement of γ from 6dFGS and this result. This change is driven by the preference for a higher Ω_m in *Planck* compared to *WMAP*.

For this analysis, we extend the range of RSD measurements used to constrain γ relative to Sánchez et al. (2013), Beutler et al. (2014), and Rapetti et al. (2013). Moreover, relative to Rapetti et al. (2013) we also use the updated *Planck* measurements as opposed to *WMAP*. The final accuracy of our measurement of the growth index improves upon Sánchez et al. (2013) and Beutler et al. (2014), given the additional measurements we analyse. Note, our constraint on the growth index disagrees with Rapetti et al. (2013) as we use different data sets, and the two measurements have similar accuracy as we choose to focus only on growth-rate measurements from RSD: we do not include additional probes sensitive to the growth rate. This position is motivated by recent suggestions that there exists some tension between the predictions from a *Planck* cosmology and RSD measurements (e.g. Macaulay, Wehus & Eriksen 2013).

6 CONCLUSIONS AND DISCUSSION

In search of departures from the standard cosmological model and clues towards possible extensions, we have measured time- and scale-dependent deviations to the gravitational field equations of General Relativity. We model these deviations using the time and scale-dependent parameters $\{G_{\text{matter}}, G_{\text{light}}\}$. These parameters are defined using 2 bins in time and 2 bins in scale. G_{matter} modifies the gravitational interaction for non-relativistic particles, and hence alters structure formation, while G_{light} acts equivalently for relativistic particles, thus affecting how light propagates through the universe.

To measure the eight parameters describing this model, plus the six describing the standard model, we utilize a range of cosmological probes including BAOs, Type Ia SNe, the CMB,
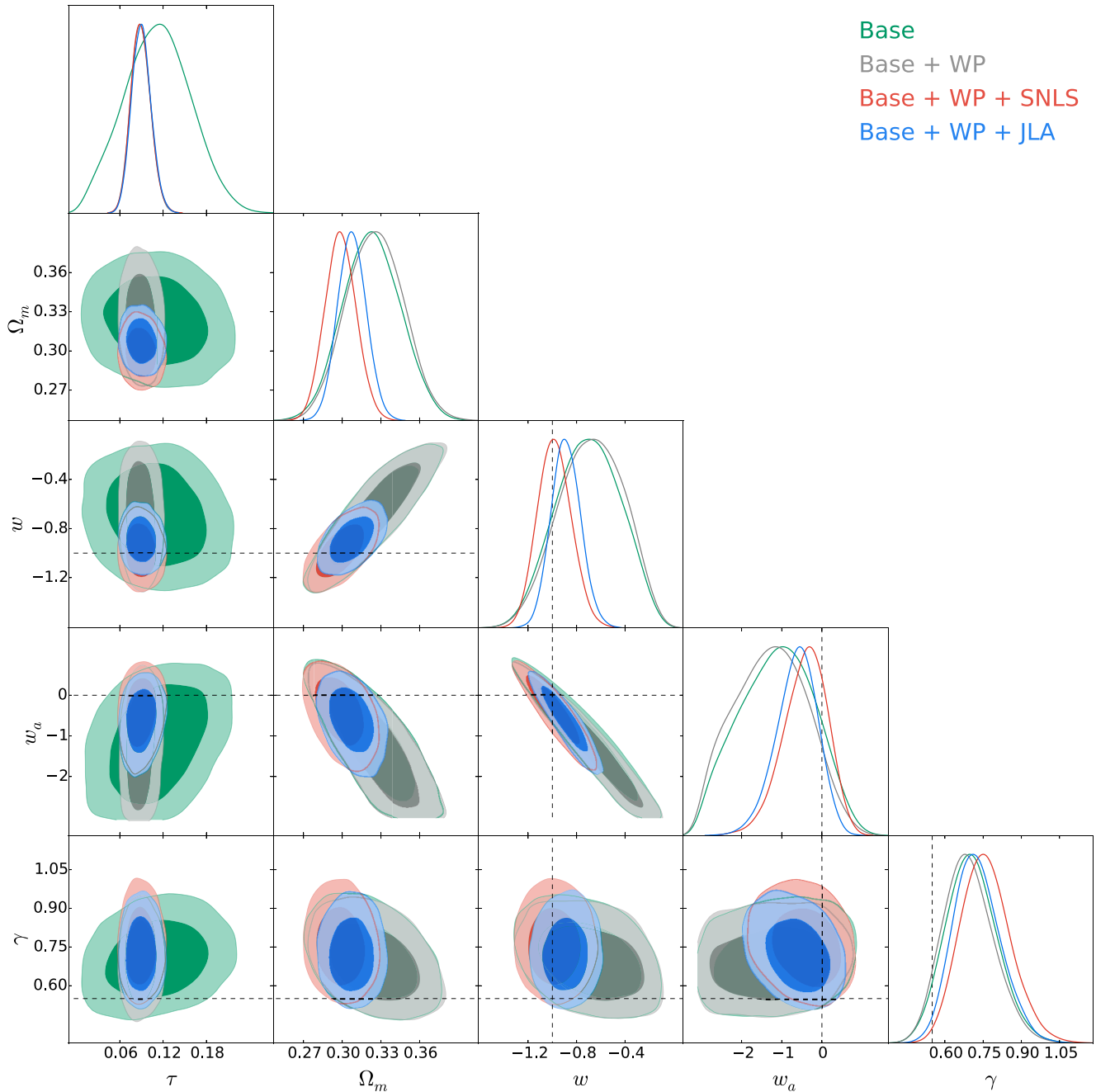
Figure 7. 68 per cent and 95 per cent confidence regions for the most relevant parameters describing model II. The base sample of data sets, as referred to above, represents the combination High-l + H_0 + RSD/AP + low-z BAO.

CMB lensing, and the cross-correlation of the CMB with large-scale structure probes. In addition, we include measurements of the power-spectrum multipoles from the WiggleZ and CMASS galaxy redshift samples, and the velocity power spectrum from 6dFGSv. Our motivation for adopting a phenomenological model is to provide a set of results that can self-consistently be used to test the widest possible range of models. To this end, we have focused on only analysing measurements on scales within the linear regime. We summarize our main results as follows.

(i) We perform a new measurement of the power-spectrum multipoles of the WiggleZ survey, featuring a new calculation of the

window function convolution effects and an improved determination of the covariance from N-body simulations.

(ii) Modelling deviation from General Relativity in terms of the growth of large-scale structure, we find the following results, given in terms of 68 per cent CL: $G_{matter}(z < 1; k > 0.01) = 0.65 \pm 0.43$, $G_{matter}(z < 1; k < 0.01) = 1.22^{+0.39}_{-0.34}$, $G_{matter}(z > 1; k > 0.01) = 0.53 \pm 0.32$, $G_{matter}(z > 1; k < 0.01) = 0.87 \pm 0.30$. These constraints are consistent with GR (i.e. $G_{matter} = 1$) at the 95 per cent confidence level. We observe a small tension ($>1\sigma$) for the high-wavenumber and high-redshift bin.

(iii) Modelling deviation from General Relativity in terms of light propagation, we derive the following constraints, given in terms

of 68 per cent CL: $G_{\text{light}}(z > 1; k > 0.01) = 1.057^{+0.053}_{-0.045}$, G_{light} $(z < 1; k < 0.01) = 1.048 \pm 0.048$, $G_{\text{light}}(z < 1; k > 0.01) = 1.153^{+0.080}_{-0.068}$, $G_{\text{light}}(z > 1; k < 0.01) = 1.016 \pm 0.026$. These constraints are consistent with General Relativity at the 95 per cent confidence level: the significant improvement in constraining power, relative to G_{matter}, is due to the sensitivity of the ISW effect and CMB lensing to deviations in G_{light}.

(iv) We preform Bayesian model comparison between general relativity and our phenomenological model. To do this we compute the evidence for both models and take the ratio. Following the scale suggested by Kass & Raftery (1995), the ratio of evidence values suggests 'no support' for modifying general relativity. This is consistent with the results from the posterior distributions.

(v) Adopting an alternative model, we introduce deviation in the expansion and growth histories simultaneously by varying the growth index and two parameters describing a redshift-dependent equation of state. For this fit we utilize, among other probes, recent growth-rate constraints from RSDs, as measured from the WiggleZ, CMASS, and 6dF surveys. Our final result assuming a ΛCDM expansion history (in terms of 68 per cent CL) is $\gamma = 0.665 \pm 0.067$, while allowing the expansion history to deviate from ΛCDM we measure $\gamma = 0.69^{+0.09}_{-0.11}$. Both these results are consistent with the standard model; however, introducing SN measurements to this fit (either SNLS or JLA) we find a $\sim 2\sigma$ tension with ΛCDM.

Probes of the velocity field of galaxies have an indispensable role to play in addressing questions of the nature of DE as they are uniquely sensitivity to only temporal perturbations. The observational data sets we have analysed are consistent with a vacuum energy interpretation of DE; however, due to the magnitude of current uncertainties any final conclusions drawn from these, and other current, observations would be premature. In future analysis tomographic weak-lensing and galaxy–galaxy lensing measurements will be included to improve our constraints; furthermore, we will begin assessing the viability of specific models using the inferred parameter constraints.

ACKNOWLEDGEMENTS

REFERENCES

Anderson L. et al., 2014a, MNRAS, 439, 83
Anderson L. et al., 2014b, MNRAS, 441, 24
Baker T., Ferreira P. G., Leonard C. D., Motta M., 2014, preprint (arXiv:e-prints)
Baldauf T., Seljak U., Smith R. E., Hamaus N., Desjacques V., 2013, Phys. Rev. D, 88, 083507
Ballinger W. E., Peacock J. A., Heavens A. F., 1996, MNRAS, 282, 877
Bean R., Tangmatitham M., 2010, Phys. Rev. D, 81, 083534
Bennett C. L. et al., 2013, ApJS, 208, 20
Bertschinger E., Zukin P., 2008, Phys. Rev. D, 78, 024015
Betoule M. et al., 2014, A&A, 568, A22
Beutler F. et al., 2011, MNRAS, 416, 3017
Beutler F. et al., 2012, MNRAS, 423, 3430
Beutler F. et al., 2014, MNRAS, 443, 1065
Beutler F., Blake C., Koda J., Marín F. A., Seo H.-J., Cuesta A. J., Schneider D. P., 2016, MNRAS, 455, 3230
Blake C. et al., 2011a, MNRAS, 415, 2876
Blake C. et al., 2011b, MNRAS, 415, 2892
Blake C. et al., 2012, MNRAS, 425, 405
Blanchard A., Schneider J., 1987, A&A, 184, 1
Bousso R., Harlow D., Senatore L., 2013, preprint (arXiv:e-prints)
Chan K. C., Scoccimarro R., Sheth R. K., 2012, Phys. Rev. D, 85, 083509
Clarkson C., Ellis G. F. R., Faltenbacher A., Maartens R., Umeh O., Uzan J.-P., 2012, MNRAS, 426, 1121
Clifton T., Ferreira P. G., Padilla A., Skordis C., 2012, Phys. Rep., 513, 1
Conley A. et al., 2011, ApJS, 192, 1
Copeland E. J., Sami M., Tsujikawa S., 2006, Int. J. Mod. Phys. D, 15, 1753
Copeland E. J., Padilla A., Saffin P. M., 2012, J. Cosmol. Astropart. Phys., 12, 26
Daniel S. F., Linder E. V., 2010, Phys. Rev. D, 82, 103523
Daniel S. F., Linder E. V., 2013, J. Cosmol. Astropart. Phys., 2, 7
Daniel S. F., Linder E. V., Smith T. L., Caldwell R. R., Cooray A., Leauthaud A., Lombriser L., 2010, Phys. Rev. D, 81, 123508
de Felice A., Kase R., Tsujikawa S., 2011, Phys. Rev. D, 83, 043515
Deffayet C., Gao X., Steer D. A., Zahariade G., 2011, Phys. Rev. D, 84, 064039
Delubac T. et al., 2014, preprint (arXiv:e-prints)
Dodelson S., 2003, Modern Cosmology. Academic Press, New York
Dossett J. N., Ishak M., Moldenhauer J., 2011, Phys. Rev. D, 84, 123001
Dossett J. N., Ishak M., Parkinson D., Davis T., 2015, preprint (arXiv:e-prints)
Efstathiou G., 2014, MNRAS, 440, 1138
Eisenstein D. J., Hu W., 1998, ApJ, 496, 605
Eriksen H. K., Jewell J. B., Dickinson C., Banday A. J., Górski K. M., Lawrence C. R., 2008, ApJ, 676, 10
Feroz F., Hobson M. P., 2008, MNRAS, 384, 449
Font-Ribera A. et al., 2014, J. Cosmol. Astropart. Phys., 5, 27
Gelman A., Rubin D., 1992, Stat. Sci., 7, 457
Gordon C., Land K., Slosar A., 2007, Phys. Rev. Lett., 99, 081301
Gubitosi G., Lagos M., Magueijo J., Allison R., 2015, preprint (arXiv:e-prints)
Hartlap J., Simon P., Schneider P., 2007, A&A, 464, 399
Hatton S., Cole S., 1998, MNRAS, 296, 10
Heymans C. et al., 2012, MNRAS, 427, 146
Ho S., Hirata C., Padmanabhan N., Seljak U., Bahcall N., 2008, Phys. Rev. D, 78, 043519
Hui L., Greene P. B., 2006, Phys. Rev. D, 73, 123526
Humphreys E. M. L., Reid M. J., Moran J. M., Greenhill L. J., Argon A. L., 2013, ApJ, 775, 13
Huterer D., Linder E. V., 2007, Phys. Rev. D, 75, 023519
Jeffreys H., 1961, Theory of Probability, 3rd edn. Oxford Univ. Press, Oxford
Joachimi B., Singh S., Mandelbaum R., 2015, MNRAS, 454, 478
Johnson A. et al., 2014, MNRAS, 444, 3926
Kass R. E., Raftery A. E., 1995, J. Am. Stat. Assoc., 90, 773
Kazin E. A. et al., 2014, MNRAS, 441, 3524
Koda J. et al., 2014, MNRAS, 445, 4267
Koda J., Blake C., Beutler F., Kazin E., Marin F., 2015, preprint (arXiv:e-prints)
Kuhn T. S., 1970, The Structure of Scientific Revolutions. University of Chicago Press, Chicago, IL
Lahav O., Massimi M., 2014, Astron. Geophys., 55, 030003
Lewis A., Bridle S., 2002, Phys. Rev. D, 66, 103511
Lewis A., Challinor A., 2006, Phys. Rep., 429, 1
Lewis A., Challinor A., Lasenby A., 2000, ApJ, 538, 473
Liddle A. R., Mukherjee P., Parkinson D., Wang Y., 2006, Phys. Rev. D, 74, 123506
Linder E. V., 2005, Phys. Rev. D, 72, 043529
Linder E. V., Cahn R. N., 2007, Astropart. Phys., 28, 481

Ma C.-P., Bertschinger E., 1995, ApJ, 455, 7

Ma Y.-Z., Gordon C., Feldman H. A., 2011, Phys. Rev. D, 83, 103002

Macaulay E., Wehus I. K., Eriksen H. K., 2013, Phys. Rev. Lett., 111, 161301

Matsubara T., Suto Y., 1996, ApJ, 470, L1

Mehta K. T., Cuesta A. J., Xu X., Eisenstein D. J., Padmanabhan N., 2012, MNRAS, 427, 2168

Padmanabhan N., Xu X., Eisenstein D. J., Scalzo R., Cuesta A. J., Mehta K. T., Kazin E., 2012, MNRAS, 427, 2132

Peacock J. A., Nicholson D., 1991, MNRAS, 253, 307

Percival W. J. et al., 2014, MNRAS, 439, 2531

Planck Collaboration XVI, 2014a, A&A, 571, A16

Planck Collaboration XV, 2014b, A&A, 571, A15

Planck Collaboration XVI, 2014c, A&A, 571, A16

Planck Collaboration XIII, 2015, preprint (arXiv:1502.01589)

Pogosian L., Silvestri A., Koyama K., Zhao G.-B., 2010, Phys. Rev. D, 81, 104023

Rapetti D., Blake C., Allen S. W., Mantz A., Parkinson D., Beutler F., 2013, MNRAS, 432, 973

Riess A. G. et al., 2011, ApJ, 730, 119

Sachs R. K., Wolfe A. M., 1967, ApJ, 147, 73

Samushia L. et al., 2014, MNRAS, 439, 3504

Sánchez A. G. et al., 2013, MNRAS, 433, 1202

Silberman L., Dekel A., Eldar A., Zehavi I., 2001, ApJ, 557, 102

Silvestri A., Pogosian L., Buniy R. V., 2013, Phys. Rev. D, 87, 104015

Simpson F., Peacock J. A., 2010, Phys. Rev. D, 81, 043512

Simpson F. et al., 2013, MNRAS, 429, 2249

Springob C. M. et al., 2014, MNRAS, 445, 2677

Susskind L., 2003, The Davis Meeting On Cosmic Inflation. Stanford University Stanford, CA, p. 26

Tassev S., Zaldarriaga M., Eisenstein D. J., 2013, J. Cosmol. Astropart. Phys., 6, 36

Trotta R., 2008, Contemp. Phys., 49, 71

Witten E., 2001, in Cline D. B., ed., Sources and Detection of Dark Matter and Dark Energy in the Universe. Springer-Verlag, Berlin, p. 27

Yamamoto K., Nakamichi M., Kamino A., Bassett B. A., Nishioka H., 2006, PASJ, 58, 93

Zhao G.-B., Li H., Linder E. V., Koyama K., Bacon D. J., Zhang X., 2012, Phys. Rev. D, 85, 123546

This paper has been typeset from a TeX/LaTeX file prepared by the author.